ELSEVIER

Atmospheric Research 84 (2007) 142–168

ATMOSPHERIC RESEARCH

www.elsevier.com/locate/atmos

Influence of wildfire induced land-cover changes on clouds and precipitation in Interior Alaska — A case study

Nicole Mölders [a,b,*], Gerhard Kramm [a]

[a] *Geophysical Institute, University Alaska Fairbanks, 903 Koyukuk Drive, P.O. Box 757320, Fairbanks, AK 99775-7320, USA*
[b] *College of Natural Sciences and Mathematics, University Alaska Fairbanks, 903 Koyukuk Drive, P.O. Box 757320, Fairbanks, AK 99775-7320, USA*

Received 13 May 2005; received in revised form 8 June 2006; accepted 8 June 2006

Abstract

As especially observed during the 2004 Alaska fire season, huge wildfires drastically alter land cover leading to a change in the dynamic (roughness length), radiative (albedo, emissivity), vegetative (vegetation type and fraction, stomatal resistance), thermal (soil heating, thawing of permafrost), and hydrological (water loss due to the fire) surface characteristics. A case study was performed with the Mesoscale Model generation 5 (MM5) assuming the landscape prior to and after the 2004 wildfires in Interior Alaska to quantitatively examine the impact of fire-caused land-cover changes on summer cloud and precipitation formation.

The results of our model study show that sensible heat fluxes into the atmosphere and air temperatures increase by up to 225 W m^{-2} and 3 K over burnt areas. Burnt areas > 600 km^2 and > 800 km^2 significantly (at the 90% or higher confidence level according to statistical tests) affect sensible and latent heat fluxes, respectively. While burnt areas must exceed 1600 km^2 for the increased buoyancy to significantly increase the upward transport of air, burnt areas > 600 km^2 already experience enough enhanced lifting to produce areas of increased cloud-water, rainwater, and graupel mixing ratios followed by an area of decreased mixing ratios downwind of them. The spatial and temporal distribution of precipitation changes appreciably and resulted in significant increases of 84 h-accumulated precipitation (by up to 15.1 mm) in the lee of burnt areas > 600 km^2, but a decrease by 0.1 mm on the domain average.

Keywords: Clouds and precipitation; Land-cover changes; Mesoscale modeling; Wildfires; Interior Alaska; MM5

1. Introduction

Lightning caused wildfires have been a natural and dominant disturbance regime in boreal forests for millennia (e.g., Stocks et al., 1998) and are an important natural component of boreal forest ecosystems (e.g., DNR, 2000). According to recent estimates 10^5 km^2, on average, burn annually in the circumpolar boreal zone (Cahoon et al., 1994) with increasing fire activity over the last three decades (Stocks et al., 2000; Podur et al., 2002). In North America, for instance, the area of boreal forest burnt annually has doubled in the last two decades (Stocks et al., 2000). Between 1940 and 2001 lightning initiated 8784 fires in Interior Alaska, and contributed 90% (based on the interval 1950 to 2001 for which a distinction was made) of the area burnt (Fig. 1). In 2004, Interior Alaska was faced with about 27,000 km^2 forest burnt, the strongest fire season since recording started in

* Corresponding author. Tel.: +1 907 474 7910; fax: +1 907 474 7290.
E-mail address: molders@gi.alaska.edu (N. Mölders).

0169-8095/$ - see front matter © 2006 Elsevier B.V. All rights reserved.
doi:10.1016/j.atmosres.2006.06.004

1940. The Boundary fire located northeast of Fairbanks burnt the largest area in 2004 with more than 2037 km^2, and was connected with the concurrently burnt area (~ 798 km^2) of the Wolf Creek fire (Fig. 2).

Fire–weather situations ensure that wildfires influence the successive development of landscapes. The succession landscapes basically show little to no biomass growth in the year of the fire, growths of moss, grass and herbs in the first three years after the fire, followed by the establishment of shrubs and saplings. About 25 to 30 years after the fire, trees densely cover the burnt area. Hardwood and spruce trees dominate about 45 to 100 years after the fire (DNR, 2000). The presence of fine fuel (e.g., grass, shrubs) may increase the mean square kilometers burnt because these plants regenerate faster than woody fuel thereby shortening the interval between burnings (Westerling et al., 2003).

In high latitudes, wildfires have become a major problem in recent years, in terms of both economics and environmental issues as industrial and recreational use of boreal forests has increased in the last century (e.g., Cahoon et al., 1994). The Boundary fire area, for instance, has a long history of fire occurrence. Canadian and Alaskan fire-management agencies recognize the ecological role of wildfires and aim to protect human life and health, cultural resources, and private property. A result of this policy is that fires in remote boreal forest substantially contribute to the nation-wide burnt area. Future fire management tasks are likely to grow because fire activity is expected to increase in response to global warming (e.g., Stocks et al., 1998).

The change in surface characteristics caused by wildfires again feeds back to climate. Boreal wildfires alter the land-surface characteristics in two ways: vegetation changes after such an event, and eventually permafrost thaws (Zhuang et al., 2003). The vegetation change leads to a decrease in surface roughness and albedo in the first years after the fire. Wildfires remove the insulating moss or peat layers. The heat generated by wildfires and conducted to permafrost soil layers (in which temperatures remain below 0 °C for at least two consecutive years) increases the thickness of the active layer (which is overlying the zone of permafrost and thaws seasonally) by thawing some of the permafrost (Zhuang et al., 2003). Results from model studies indicated that variations in soil moisture and vegetation can strongly influence precipitation (e.g., Chang and Wetzel, 1991).

Intensely burnt areas can still be distinguished from moderately burnt areas many years after a fire in Advanced Very High Resolution Radiometer (AVHRR) imagery (e.g., Cahoon et al., 1994). The surface of burnt regions in the Canadian boreal forest, for instance, was up to 6 K warmer than surrounding areas and remained warmer even 15 years after the fire (e.g., Amiro et al., 1999). These changes caused by wildfires alter the thermal and hydrological regime of the soils. According to aircraft measurements, sensible heat fluxes into the atmosphere increase about 10 to 20% for the first few years after the fire, while latent heat fluxes slightly decrease causing the Bowen ratio (=sensible heat flux/latent heat flux) to increase by about 50% (e.g., Amiro et al., 1999). However, Liu et al. (2005) measured components of the surface energy flux budget for a 1-year period starting on April 10, 2002 for three large burn scars in Interior Alaska resulting from fires in 1999, 1987, and circa 1920. These three sites were classified by the authors as a 3-year site primarily covered with bunch grasses, a 15-year site primarily covered with aspen and willow, and an 80-year site primarily covered with black spruce, respectively. Annual net radiation declined by 31% for both the 3- and the 15-year sites as compared with the 80-year site (which had an annual mean of 55 W m^{-2}); Annual sensible heat fluxes were reduced by 55% at the 3-year site and by 52% at the 15-year site as compared with the 80-year site (which had an annual mean of 21 W m^{-2}). At the 3-year site annual evapotranspiration (i.e., evaporation plus transpiration) decreased by 33% as compared with the 80-year site (which had an annual mean of 301 mm/y); at the 15-year site it was approximately the same (283 mm/y) as that from the 80-year site, even though the 15-year site had substantially higher evapotranspiration during July. Liu et al. (2005) also stated that the absolute differences between the post-fire ecosystems and the mature black spruce forest for both net radiation and sensible heat fluxes were the greatest during spring (because of differences in snow cover and surface albedo), substantial during summer and winter, and relatively small during fall. Obviously, the different temporal and spatial scales of observations are responsible for the different empirical findings of the aforementioned studies.

The fire regime is sensitive to (1) previous weather conditions (e.g., Stocks et al., 1998, 2000; Hess et al., 2001; Hoadley et al., 2004) and (2) the frequency of lightning. Lightning activity depends on charge separation and transfer caused by graupel and updraft formation (e.g., Houze, 1993). Instability and moisture availability are critical determinants of the development of convective clouds and precipitation severity (Crook, 1996), while the updraft strength affects graupel formation (Berdeklis and List, 2001) and frequency of lightning (Fehr et al., 2003). Thus, alteration in the strength of updrafts and amount and/or frequency of graupel may affect the number of lightning strikes and wildfires.

Various observations have presented evidence that land surface contrasts may cause mesoscale atmospheric circulations and/or affect clouds and precipitation and their distribution (e.g., Changnon, 1980; Rabin et al., 1990; Bougeault et al., 1991; Mahrt et al., 1994; O'Neal, 1996). Several modeling studies carried out with real or artificial landscapes support these observational findings (e.g., Anthes, 1984; Pinty et al., 1989; Ziegler et al., 1995, 1997; Avissar and Liu, 1996; Mölders, 2000a; Weaver and Avissar, 2001; Trier et al., 2004). Differences in land surface characteristics result in small differences in boundary layer temperature and moisture. Such variations, even if they are within the range of observational errors (1 K, 1 g/kg), can be decisive for no initiation or development of intense convection (Crook, 1996). While clouds and precipitation appear randomly in homogeneous landscapes, a landscape structure can trigger mesoscale circulations and increase the amount of water that can be condensed and precipitated (e.g., Anthes, 1984; Avissar and Liu, 1996; Friedrich and Mölders, 2000). The horizontal distribution of sensible heating plays an important role for convection development (e.g., Peckham and Wicker, 2000). Obviously, the patch of similar land-cover must exceed several kilometers and large-scale flow conditions must be favorable to produce a discernable response of the atmosphere (e.g., Shuttleworth, 1988; Mölders, 1999a; Doran and Zhong, 2000; Peckham and Wicker, 2000; Peckham et al., 2004). To resolve the atmospheric response of processes to land cover differences in numerical models, land cover must be the same in several adjacent grid-points (e.g., Pielke, 2001; Noppel and Fiedler, 2002; Mölders and Olson, 2004).

Recent studies showed that under favorable weather conditions (moderate large-scale flow) land-cover changes exceeding 50 km^2 cause greater changes in cloud and precipitation formation in landscapes dominated by forest than in those dominated by agriculture (Mölders, 1999b). Boreal wildfires like those in Interior Alaska in 2004 cause extended patches in a relatively homogeneous, forest dominated landscape. Hitherto, knowledge about the effects of wildfire-caused land-cover changes on regional cloud and precipitation formation in Sub-Arctic landscapes has been limited.

In the real world, experiments are rarely repeatable under identical conditions. This is especially true when field experiments could be responsible for substantial damage, such as burning a forest as a test area. Consequently, field experiments are not well suited for answering questions about the consequences of major burnt areas for cloud and precipitation formation. Therefore, we turn to numerical modeling techniques to examine the effect of the new surface characteristics established after the 2004 fire disturbance on cloud and precipitation formation. To achieve this goal, we have chosen a weather situation, typical for convective situations in Interior Alaska during summer, for our model experiments that alternatively employ the land-cover data of the landscape prior to and after the huge wildfires of the 2004 Alaska fire season. The latter are considered because they permit a realistic estimate of possible land-cover changes during an Alaska fire season. The influences of wildfire-induced land-cover changes on clouds and precipitation are analyzed by comparing the results of the model predictions alternatively performed. Such an analyzing procedure is widely accepted in numerical studies on land-cover changes and their impact on the atmosphere (e.g., Copeland et al., 1996; Xue, 1996; Chase et al., 1999; Pan et al., 1999; Pielke et al., 1999; Taha, 1999; Mölders, 2000a). To achieve our goal, a simulation of the spread of wildfires is, of course, not necessary.

2. Brief description of the model and initialization

2.1. Model set-up

We apply the mesoscale meteorological model MM5 (e.g., Dudhia, 1993; Grell et al., 1994; Reisner et al., 1998; Thompson et al., 2004) of the Pennsylvania State University and the National Center for Atmospheric Research (NCAR), well validated by many authors (e.g., Oncley and Dudhia, 1995; Manning and Davis, 1997; Colle et al., 1999; Mölders, 2000b; Bromwich et al., 2001; Cassano et al., 2001; Chen and Dudhia, 2001; Hoadley et al., 2004; Mölders and Olson, 2004; Narapusetty and Mölders, 2005).

Cloud-microphysical processes are simulated by the five water class (cloud-water, rainwater, ice, snow, graupel) cloud scheme, the so-called Reisner-2 option (Reisner et al., 1998), substantially improved and applied by Thompson et al. (2004) to evaluate the sensitivity of winter precipitation to numerous aspects of a bulk, mixed-phase microphysical parameterization. This parameterization permits cloud-water and ice to coexist at temperatures below freezing. Recently, Lynn et al. (2005a,b) implemented a spectral (bin) microphysics in MM5 and assessed the predictions of the original and improved Reisner-2 scheme with the results of the spectral microphysics scheme for a CaPE (**C**onvection **a**nd **P**recipitation/Electrification **E**xperiment) rain event with a squall-line. These authors found that the upgraded Reisner-2 scheme provided improved rainfall, but not improved cloud structure.

Dudhia's (1989) simple radiation scheme is considered. The turbulent transfer processes are parameterized in accord with Hong and Pan (1996). Soil and vegetation processes are described by the Hydro-Thermodynamic Soil–Vegetation Scheme (HTSVS) (e.g., Kramm et al., 1994, 1996; Mölders et al., 2003a; Mölders and Walsh, 2004).

2.2. Land surface model

The HTSVS predicts the exchange of momentum, sensible heat, and moisture at the vegetation–soil–atmosphere interface with special consideration of heterogeneity on the micro-scale by the mixture approach, as suggested by Deardorff (1978). It consists of a multi-layer soil model, a single-layer canopy model (Kramm et al., 1994, 1996; Mölders et al., 2003a) and a multi-layer snow-model (Mölders and Walsh, 2004). Based on the governing balance equations for heat and moisture (e.g., Philip and de Vries, 1957; de Vries, 1958; Sasamori, 1970; Sievers et al., 1983; Flerchinger and Saxton, 1989; Kramm et al., 1994, 1996; Mölders et al., 2003a), the multi-layer soil model predicts (1) infiltration, (2) the vertical heat conduction and the vertical transfer of water vapor and liquid water (i.e., the Richards-equation is always embedded), (3) freezing/thawing of frozen ground, (4) cross-effects such as the Ludwig–Soret effect (i.e., a temperature gradient contributes to the water flux and changes the soil liquid volumetric water content) and the Dufour effect (i.e., a moisture gradient contributes to the heat flux and, hence, alters soil temperature) that are formulated in the sense of the linear thermodynamics of irreversible processes (e.g., de Groot, 1951; Prigogine, 1961), (5) the related release and consumption of energy due to phase transition, (6) water uptake by plants, including a variable vertical root distribution, dependent on vegetation type, and (7) the temporal variation of soil albedo. Note that soil water vapor fluxes become important during a wildfire as at temperatures higher than 100 °C no liquid water exists.

Comparison of simulated and observed data of wind speed, temperature, and humidity, and of eddy fluxes of momentum, sensible heat, and water vapor of the Great Plains Turbulence Project and GREIV I-1974 (**GRE**nzschicht **I**nstrumentelle **V**ermessung), CASES97 (**C**ooperative **A**tmosphere **S**urface **E**xchange **S**tudy 1997) and BALTEX (**BALT**ic sea **EX**periment) showed that HTSVS accurately simulates the diurnal course of state variables and fluxes (e.g., Kramm, 1995; Mölders, 2000b; Narapusetty and Mölders, 2005). It acceptably captures the diurnal cycle of soil temperatures, and predicts soil temperatures within 1–2 K accuracy, on average (e.g., Kramm, 1995; Mölders, 2000b; Narapusetty and Mölders, 2005). By using lysimeter data Mölders et al. (2003a,b) found that HTSVS predicts the long-term (2050 d) accumulated sums of evapotranspiration and recharge with better than 15% accuracy.

2.3. Model domain

The model domain (Fig. 2) covers 203,000 km^2 with 116 × 70 grid-points, using a horizontal grid increment of 5 km, and 23 vertical layers reaching to 100 hPa. Seven layers are below 1 km height; the first layer above the ground is about 30 m thick. The tops of the model layers are at sigma levels 0.025, 0.075, 0.175, 0.225,

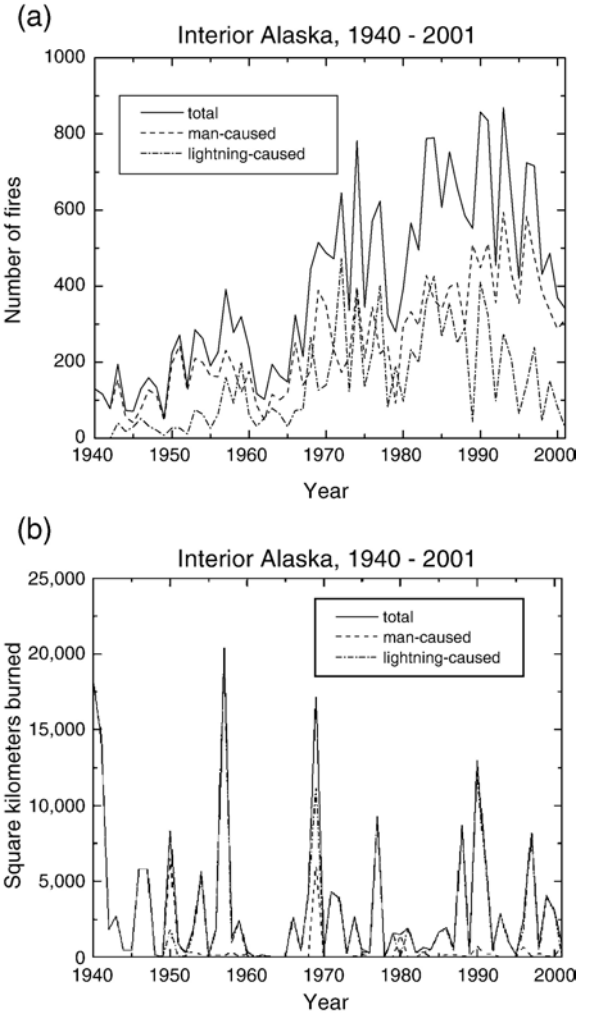

Fig. 1. Statistics on fire in Interior Alaska (a) number of fires that occurred in Interior Alaska from 1940 to 2001, caused by human and lightning, and (b) areas burnt in Interior Alaska from 1940 to 2001 (both with reference to Gabriel and Tande, 1983; S. Christensen, BLM-Alaska, 2002, personal communication).

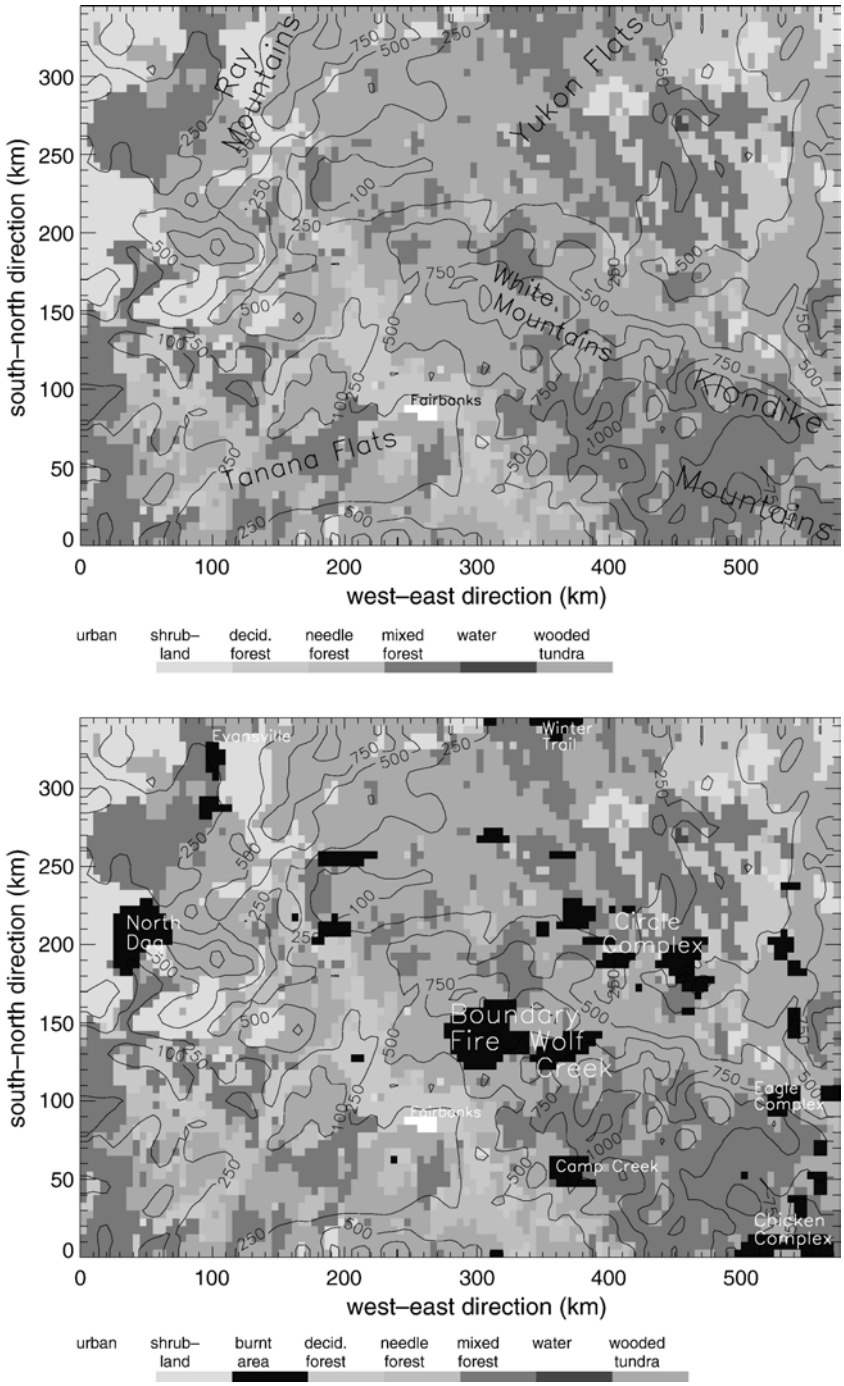

Fig. 2. Model domain setup of this study (a) original landscape (CTR) and (b) landscape after the fires (BRN). Gray shades and contour lines give the land cover and terrain elevation in the model. Names refer to locations mentioned in the text.

0.275, 0.325, 0.375, 0.425, 0.475, 0.525, 0.575, 0.625, 0.675, 0.725, 0.775, 0.825, 0.87, 0.91, 0.945, 0.97, 0.985, 0.995, and 1. This grid spacing is a compromise between the existing limitations on land-cover data and simulating the region of interest with high enough resolution to capture mesoscale processes. Interior Alaska is mainly covered by large extended forest (cf. Fig. 2), and the only city, Fairbanks (30,224 inhabitants; 83.64 km^2,

Table 1
Soil profile characteristics used in our study

Soil-type	k_s (10^{-4} m/s)	η_s (M^3/m^3)	b	ψ_s (M)	$c_S\rho_S$ (10^6 J m^{-3} K^{-1})	ε_g
Loamy sand	1.563	0.410	4.38	−0.090	1.41	0.95
Sandy loam	0.341	0.435	4.90	−0.218	1.34	0.95
Loam	0.070	0.451	5.39	−0.478	1.21	0.95
Clay loam	0.025	0.476	8.52	−0.630	1.23	0.95
Clay	0.013	0.482	11.40	−0.405	1.09	0.95

Here, k_s, η_s, b, ψ_s and $c_S\rho_S$ are the saturated hydraulic conductivity, volumetric water content at saturation (porosity), pore-size distribution index, saturated water potential, and volumetric heat capacity of the dry soil material. Parameters are from Clapp and Hornberger (1978), Cosby et al. (1984), and Pielke (2001). Furthermore, ε_g is the emissivity of the ground.

US Census Bureau, 2000), is not included at the finest grid spacing at which datasets are available despite the fact that it should be resolvable at that scale.

The uppermost soil-layer ranges from the earth's surface to the uppermost level within the soil at 0.1 m depth. Between that level and the lowest level at 2.95 m depth, there are four layers spaced by the same logarithmic increment so that central differences can be used in solving the coupled soil temperature and moisture equations by a generalized Crank–Nicholson scheme. The time step is 15 s.

2.4. Input data and initialization

A convective weather situation, as frequently occurs for Interior Alaska during summer, is considered for our model experiment. The simulations cover July 20, 0000 UT, to July 23, 1200 UT, 2001. The National Centers for Environmental Prediction/NCAR Reanalysis (NNR) data serve as initial and boundary conditions. The vegetation fraction of each grid-cell is a weighted combination of the July and August monthly five-year mean green vegetation cover data (0.15° resolution) derived from AVHRR data (Gutman and Ignatov, 1998). The 1-km resolution US Department of Agriculture (USDA) State Soil Geographic Database (Miller and White, 1998) and 10-min resolution US Geological Survey (USGS) terrain and vegetation data provide the soil texture, terrain elevation, and land-cover type. As Fairbanks is not included in the common dataset, it was introduced at its location (Fig. 2) because it extends more than a grid cell of 25 km^2. Tables 1 and 2 list the soil physical and plant parameters used in our model study.

Initial total soil moisture and temperatures are interpolated from the NNR data. The partitioning between the solid and liquid phase follows Mölders and Walsh (2004). Since the HTSVS works for both the permafrost and active layer, no assumptions on active layer depth are required. At the bottom of the soil model, soil temperature, volumetric water and ice content remain constant throughout the simulation.

2.5. Synoptic situation

The beginning of the period was characterized by moderate southerly flow over south and southwest Alaska caused by cyclonic activity within a large-scale trough over the north Pacific and Bering Sea. An upcoming ridge led to an increase in geopotential height over eastern Interior Alaska and western Canada. In the next 12 h, the ridge continued building up. The eastward propagating long-wave disturbance slightly deepened and turned the southerly flow on its frontal edge into the dominant feature over Alaska. In the middle and towards the end of the episode, a weak trough influenced the synoptic situation. The reinforcement of the cyclonic activity remnants in the Aleutians resulted from the cold advection on the back edge of the trough. On July 23, the anti-cyclonic circulation over western Canada strengthened, while the low-pressure field dominating Alaska gradually cut off.

In the first half of the period the cyclone located in the Bering Sea gradually dissipated, thereby weakening the southerly flow over Alaska at the surface. Alaska remained on the outer edge of a well-developed eastward moving surface cyclone located over North Siberia for the rest of the time. This weather situation led to southwesterly wind directions in the lower Atmospheric Boundary Layer (ABL) in the first 34 h. Between the 34th and 60th hour, winds are from northeast in the southern part of Interior Alaska, followed by about 8 h of transition back to a southwestern regime. The southwestern wind remains until the end of the episode.

Strong convection developed in Interior Alaska, and near-surface air and dew-point temperatures ranged from 8 to 22 °C, and −1 to 16 °C at low elevation, respectively. At this time of the year, sun rises (sets) around 0400 (2330) Alaska Standard Time (AST), which is UT minus 9 h.

3. Experimental design

3.1. Numerical experiments

Simulations were performed alternatively using the land-cover data of the landscape prior to and after the fires (Fig. 2). These simulations were carried out for the pre-

(control) and after-fire (burnt) landscape; their results are denoted CTR and BRN, hereafter. All predictions were performed without any form of nudging to meteorological analysis or observational data, to simulate a real time environment where such observations are not available through the entire forecast period.

The land-cover data for the BRN landscape was created from the original land-cover data by marking the grid-points as "burnt areas" according to areas burnt in Interior Alaska during the 2004 fire season. Data on square kilometers and locations burnt were derived from maps and information provided by the Alaska Interagency Coordination Center. Burnt areas extending less than 25 km^2 are of subgrid-scale with respect to the model grid. A fire must have annihilated, at least, 12.5 km^2 of the original landscape to show up as a "burnt area" grid element.

From a physical point of view, in our BRN simulation burnt areas were realized by altering the respective surface properties (empirical parameters) of the grid-cells representing the pre-fire landscape to those usually found after burning (Table 2). Burnt areas, for instance, are considered to be partly covered by grass because grass is the first to grow in these areas four to six weeks after a fire event (DNR, 2000). Burnt areas, among other things, mean a decrease of albedo (e.g., Cahoon et al., 1994; Amiro et al., 1999) and aerodynamic roughness as compared to the pre-fire situation. As reported by Beringer et al. (2003), soil albedo of burnt areas amounts to about 0.06 to 0.07. Thus, in BRN soil albedo is set equal to 0.07 and treated as not dependent on soil moisture η in the burnt areas because usually 2–5 cm ashes and charred organic material remain above the mineral soil (Chambers et al., 2005). We assume vegetation fractions of burnt areas to be only 10% ($0.1\sigma_f$) of the fractions σ_f these areas had in the same grid-cell in CTR, and that the first grass growing on these areas has an albedo of 0.13 (Table 2). Since in non-burnt area grid-cell albedo ($\alpha_{grid\text{-}cell}=\alpha_f\sigma_f+(1-\sigma_f)\alpha_g(\eta)$) depends on vegetation fraction σ_f, vegetation albedo α_f and the soil-moisture dependent soil albedo $\alpha_g(\eta)$, and because albedo of the darkest soil condition (saturated soil) is higher than that of the ashes (α_{ash}), the albedo of a burnt area is always lower than that of the original area ($\alpha_f\sigma_f+(1-\sigma_f)\alpha_g(\eta)>\alpha_f\sigma_f\,0.1+(1-\sigma_f\,0.1)\alpha_{ash}$).

Clearly, fires heat the soil. Thus, huge amounts of soil water evaporate during the fire. In permafrost areas, the fire-induced change in soil temperature is accompanied by an alteration of the total soil water content and the partitioning of the water phases (see, e.g., Hinzman et al., 2003). Moreover, infiltration, soil volumetric heat capacity and hydraulic conductivity of unfrozen, partly frozen and frozen ground differ appreciably. As compared to the pre-fire conditions, burnt areas show a shift towards warmer soil regimes, i.e., the hydro-thermodynamic state of soil is lastingly affected by fires. To realize this effect in the attempt to initiate our BRN simulation reasonably, we performed offline simulations with the HTSVS assuming near-surface air temperatures of, on average, 600 K, and a wind speed of 15 m/s at the same height for two consecutive days (48 h). The altered wind speed recognizes that upward and downward motions strongly increase and horizontal circulations develop in response to the fire (e.g., Coen et al., 2004).

Table 2
Plant specific parameters (from Pielke, 2001; Wilson et al., 1987; Jackson et al., 1996)

Land-cover type	$r_{st,min}$ (s/m)	ψ_c (m)	m (kg/m^2)	a	R_r (10^{-4} m)	b_{st}	T_{min} (°C)	T_{max} (°C)	T_{opt} (°C)	α_f	ε_f	z_{root} (m)	z_0 (m)
Urban	200	−255	20	0.02	3.5	50	5	45	25	0.25	0.85	2.9	1
Shrubland	300	−133	4.8	0.36	2.51	10	5	45	25	0.25	0.95	2.0	0.03
Deciduous forest	100	−214	1.2	0.02	3.5	22	10	45	25	0.12	0.95	2.0	0.80
Needleleaf forest	125	−163	12.7	0.02	3.5	25	−5	35	25	0.10	0.97	2.0	1.09
Mixed forest	125	−158	8.2	0.02	3.5	23	0	40	25	0.12	0.96	2.0	0.8
Water	–	–	–	–	–	–	–	–	–	0.05	0.993	–	0.0001
Wooded tundra	150	−163	15.5	0.4	3.5	40	5	40	25	0.16	0.97	1.81	0.06
Burnt areas	70	−92	2.4	0.24	0.925	20	5	45	9	0.13	0.9	0.3	0.025

Here, $r_{st,min}$, ψ_c, m, a, R_r, b_{st}, T_{min}, T_{max}, T_{opt}, α_f, ε_f, and z_{root} are the minimum stomatal resistance, the water potential at which the production of cytokinins by roots is sufficiently reduced to close stomata, the fine root (ovendry) biomass, the partitioning of roots between the upper and lower root zone, the mean root radius, a parameter used to calculated stomatal resistance r_{st}, the temperature at which stomata close, the temperature at which r_{st} reaches its minimum, the albedo and emissivity of vegetation foliage or water, and the maximum root depth, respectively. Note that a grid-cell can be partly covered by vegetation, and soil albedo depends on soil volumetric water content independent of land cover type except for "burnt area". Here the value given is the albedo of the grass growing on these areas. The fraction of burnt areas that is not covered by grass is assumed to be covered by ashes having an albedo of 0.07 (see text for details). Average volumetric density of roots (oven dry) is set to 500 kg/m^3. In accord with Dingman (1994) field capacity and wilting point are the volumetric water content for which water potential drops to −3.4 and −150 m. Roughness length for burnt areas was estimated as $0.1\cdot z_h$ (e.g., Oke, 1978) where z_h is the average canopy height of the burnt area.

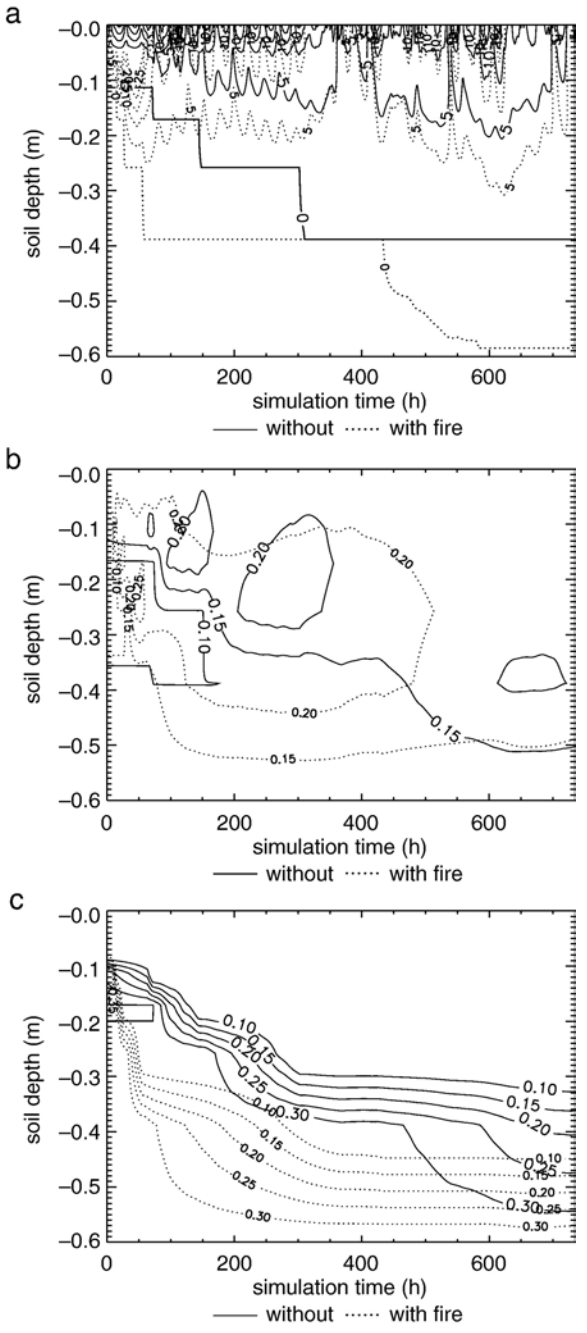

Fig. 3. Example of temporal evolution of (a) soil temperatures (°C), (b) volumetric water ($m^3\ m^{-3}$) and (c) ice content ($m^3\ m^{-3}$) during (first 48 h of the offline simulations) and after fire (see text for details). A typical summer forcing is assumed over silt loam. "Steps" are due to the vertical grid spacing of the soil model. Other soils show similar behavior.

The wind value chosen is on the lower range of those observed during FROSTFIRE; observed temperature ranged between 300 to 800 °C (Coen et al., 2004). We continued the offline simulation assuming normal summer weather conditions, but modified surface characteristics for four weeks (e.g., Fig. 3). A further offline simulation assuming the same meteorological, but pre-fire surface conditions for the entire simulation time provided the reference profiles of soil temperature, volumetric water and ice content. The differences obtained serve to reasonably initialize soil temperature and moisture states below the fire scars in BRN. At 0.05, 0.13, 0.32, and 0.80 m depth (used in MM5 to predict soil quantities), soil temperatures were, on average, about 3.1, 1.9, 2.1, and 1.6 K higher for the simulations assuming a fire than for the reference simulation (e.g., Fig. 3), and total volumetric water (liquid plus solid) content reduced to 86.4, 83.1, and 80.4% of the original values in the uppermost three soil layers. The upper two layers belong to the active layer that is already thawed at this time of the year. In the third layer, in which permafrost occurs prior to the fire, the frozen ground thawed completely, i.e., the active layer thickness grows due to the fire. As also observed during FROSTFIRE (Hinzman et al., 2003), liquid water content increases slightly deeper beneath the surface in the active layer because frozen ground thawed during the fire (e.g., Fig. 3). Sensitivity studies with longer fire duration led to higher temperatures especially in the upper soil. Based on additional sensitivity studies performed with longer periods after the fire event, a very slow decrease in the fire-enhanced soil temperatures especially in deeper soil layers was analyzed.

In MM5, initial soil temperature and moisture profiles were adjusted to after-fire conditions for BRN as follows: In recognizing the results from the offline simulations with the HTSVS, initial soil temperatures obtained from the NNR data were increased by adding the differences in soil temperature, and by lowering the total volumetric water content to the respective percentages in each burnt-area grid element. Then total soil water content was partitioned between the liquid and solid phase in accord with Mölders and Walsh (2004).

Infiltration is calculated by an explicit formulation of the Green-and-Ampt-approach in accord with Schmidt (1990) (Mölders et al., 2003a). Since infiltration depends on the water content at onset of precipitation and precipitation rate, the different soil moisture conditions of the original and burnt areas and differences in precipitation distribution affect infiltration rates.

3.2. Analysis

The weather situation simulated here occurred prior to the wildfires and is an exemplary situation for producing

Table 3
Performance measures, bias $\bar{\phi}$, root mean square error RMSE, standard deviation of error SDE, and correlation coefficient R as obtained for CTR

Skill score	Quantity	Time after start of simulation							
		0	12	24	36	48	60	72	84
$\bar{\phi}$	T (K)	0.0	0.2	0.2	0.1	−0.1	−0.1	0.1	0.1
	q_v (g/kg)	0.0	0.004	0.056	0.009	0.028	−0.053	0.097	−0.065
	$\|v\|$ (m/s)	0.0	−0.38	0.52	0.13	0.31	−0.20	0.17	0.04
RMSE	T (K)	0.0	0.3	0.5	0.3	0.4	0.4	0.3	0.3
	q_v (g/kg)	0.0	0.131	0.162	0.136	0.194	0.265	0.266	0.323
	$\|v\|$ (m/s)	0.0	1.00	0.92	0.52	0.79	0.65	0.63	0.73
SDE	T (K)	0.0	0.3	0.4	0.3	0.4	0.4	0.3	0.3
	q_v (g/kg)	0.0	0.131	0.152	0.135	0.192	0.260	0.247	0.316
	$\|v\|$ (m/s)	0.0	0.93	0.759	0.508	0.732	0.616	0.607	0.726
R	T (K)	1.000	0.999	0.999	0.999	0.999	0.999	0.999	0.999
	q_v (g/kg)	1.000	0.999	0.998	0.999	0.998	0.997	0.997	0.997
	$\|v\|$ (m/s)	1.000	0.993	0.994	0.998	0.994	0.992	0.991	0.955

Simulation starts on 20 July at 0000UT.

precipitation from local recycling of water. For confidence in the results of our study, the hypothesis is tested that temperature, specific humidity and wind speed predicted by CTR do not differ significantly (at the 95% confidence level) from the corresponding NNR data. In the comparison of CTR with the NNR data the term "significant" will only be used if the differences pass a Student's t-test at the 95% or higher confidence level.

Moreover, performance measures (e.g., Anthes, 1983; Anthes et al., 1989; Hanna, 1994) including the correlation coefficient, percent fraction of cases where the prediction is within a factor of 2 of the analysis, bias

$$\bar{\phi} = \frac{1}{n}\sum_{i=1}^{n} \phi_i, \tag{1}$$

root-mean-square error

$$\mathrm{RMSE} = \left(\frac{1}{n-1}\sum_{i=1}^{n} (\phi_i)^2\right)^{1/2}, \tag{2}$$

and the standard deviation of error

$$\mathrm{SDE} = \left(\frac{1}{n-1}\sum_{i=1}^{n} (\phi_i - \bar{\phi})^2\right)^{1/2} \tag{3}$$

are calculated using the CTR and NNR data. Here ϕ_i is the difference between the ith prediction and analysis value and n is the total number of grid points. The bias gives the systematic error resulting from consistent misrepresentation of physical, geometrical, and numerical factors. The RMSE evaluates the overall performance. The SDE indicates random errors due to uncertainty in initial and boundary conditions or the NNR data.

In accord with Weaver and Avissar (2001), predicted cloud distributions are evaluated using data collected during various passages of NOAA-12 and NOAA-14 AVHRR. There are data available for Interior Alaska from 12 passages. Note that due to the high-latitude location of Interior Alaska often two passages are close apart in time (e.g., 21 July 2001 1619UT and 1637UT).

Since Interior Alaska is sparsely populated (0.04 inhabitants/km^2 = 1 inhabitant/grid element), only seven so-called first class precipitation stations exist in the model domain, most of them located in the vicinity of Fairbanks. To increase the number of observations and spatial coverage, data from 21 additional sites run by volunteers have been included. The data gained at these sites may be of limited quality and observational times differ among sites. Nevertheless, simulated and observed 24-hour accumulated precipitation is compared for the respective observational intervals for grid cells in which a site is located.

The investigation of the impact of burnt areas on cloud and precipitation is focused on the differences in (1) near-surface fluxes of sensible and latent heat, (2) cloud extension, location and composition, and (3) precipitation distribution and amount. Domain-averages

Fig. 4. Comparison of MM5 simulated vertically integrated cloud-water content at (a) 21 July 2001 0200UT after 26 h of simulation, (c) 21 July 2001 1600UT after 40 h of simulation and (e) 23 July 2001 0200UT after 74 h of simulation, and NOAA-12 AVHRR images for (b) 21 July 2001 0236UT, (d) 21 July 2001 1619UT, and (f) NOAA-14 AVHRR image for 23 July 2001 0223UT.

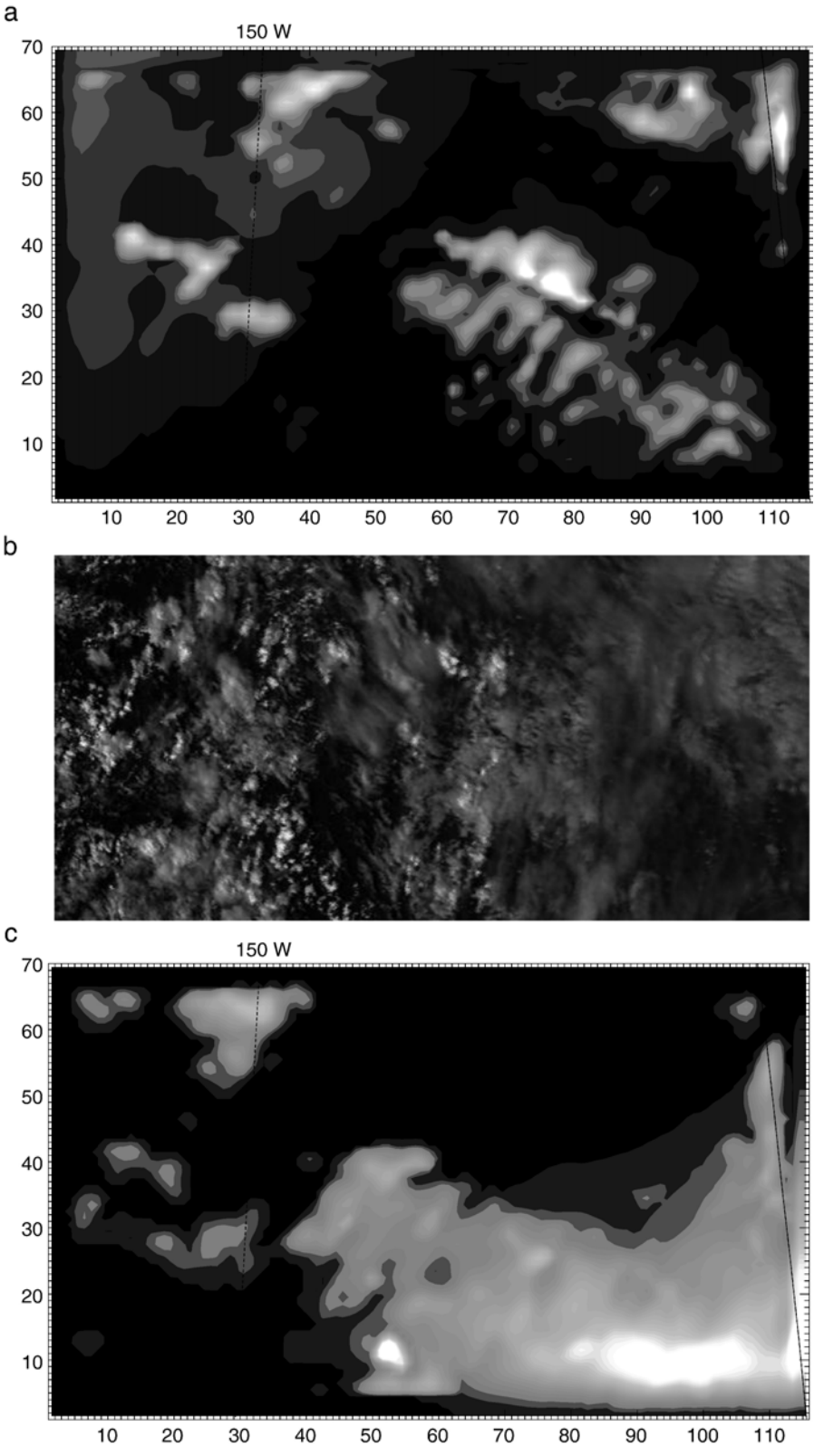
a
150 W
70
60
50
40
30
20
10
10 20 30 40 50 60 70 80 90 100 110
b
c
150 W
70
60
50
40
30
20
10
10 20 30 40 50 60 70 80 90 100 110

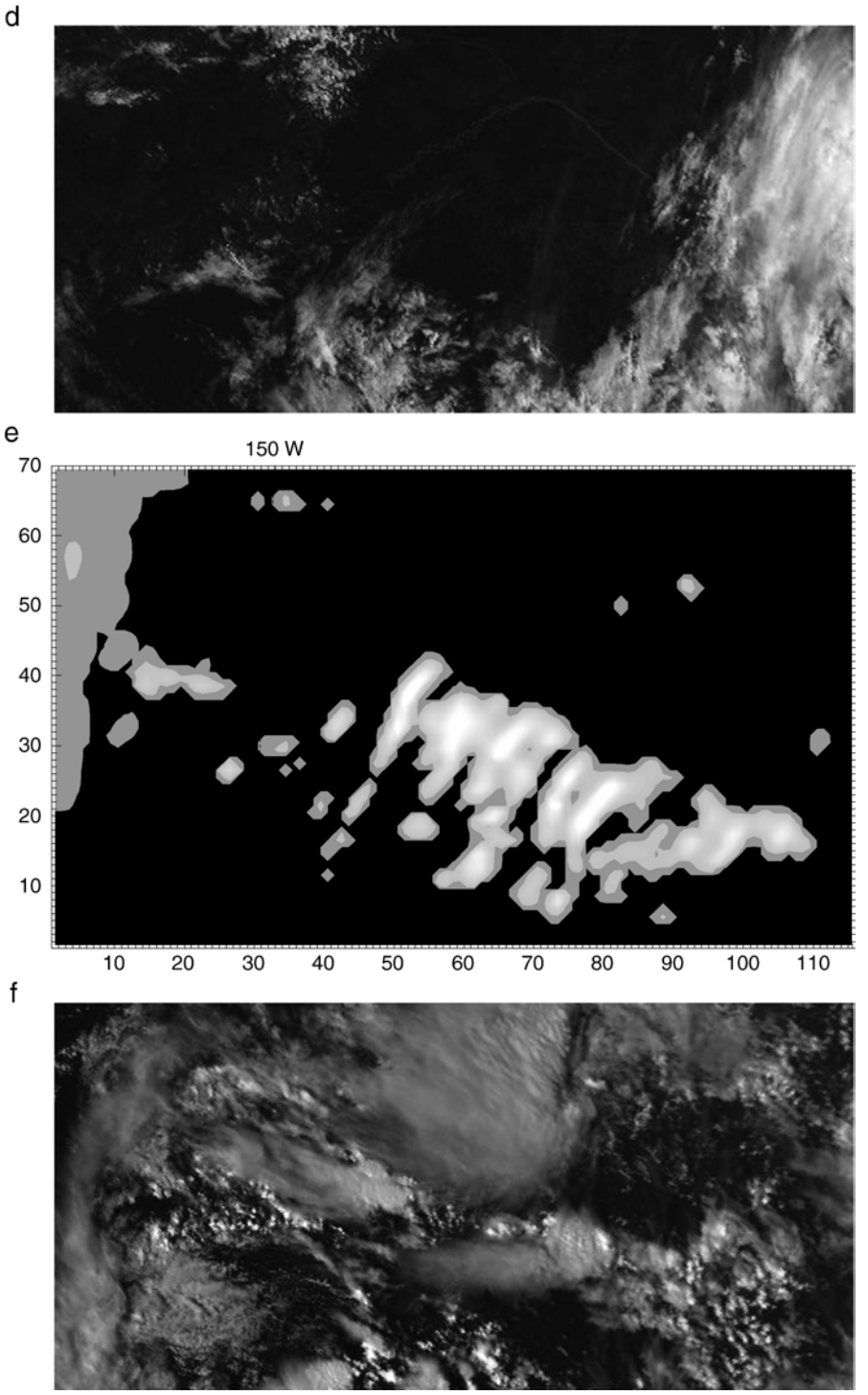

Fig. 4 (*continued*).

serve to evaluate the impact for the Interior Alaska region. For each grid point and the domain average, the probability that CTR and BRN have significantly different variances is examined by an F-variance test

$$F = \frac{\sum_{j=1}^{n}\left(x_{\mathrm{CTR},j}-\bar{x}_{\mathrm{CTR}}\right)^2-\frac{1}{N}\left(\sum_{j=1}^{n}\left(x_{\mathrm{CTR},j}-\bar{x}_{\mathrm{CTR}}\right)\right)^2}{\sum_{j=1}^{n}\left(x_{\mathrm{BRN},j}-\bar{x}_{\mathrm{BRN}}\right)^2-\frac{1}{N}\left(\sum_{j=1}^{n}\left(x_{\mathrm{BRN},j}-\bar{x}_{\mathrm{BRN}}\right)\right)^2} \quad (4)$$

Here n refers to the total number of hours. In the comparison of CTR and BRN, the term "significant" will be only used to denote CTR and BRN or their variances being different at the 90% or higher confidence level. Moreover, for the burnt areas state variable and flux averages, called area-averages hereafter, are calculated for both CTR and BRN to assess the mean change over burnt areas.

4. Evaluation of CTR

4.1. Weather analysis data

The hypothesis that the fields of temperature, wind and specific humidity predicted by CTR do not differ significantly (at the 95% confidence level) from those of the NNR data has been confirmed by tests customarily considered in statistical applications in atmospheric sciences. All performance skills show a slightly better performance at night than by day (Table 3). The relative scatter is negligibly small (therefore not shown). Simulated wind and specific humidity correlate well with the respective NNR data ($R \geq 0.995$) and are within a factor of 2 in more than 99.6 and 97.5% of the cases, respectively. The bias of the fields of temperature, specific humidity and wind speed are within the range of measurement errors (Table 3) indicating that systematic errors are small over and at the end of the period. The RMSEs (Table 3) are low and within the range of routine radiosonde-data errors (Lorenc et al., 1996). The SDEs indicate the presence of only slight random errors due to initial and boundary conditions or the NNR data (Table 3). Based on these investigations MM5 well simulates the weather situation of our study.

4.2. Satellite data and precipitation amounts

Comparison of simulated vertically integrated cloud content and the corresponding satellite imagery substantially agree except for a slight temporal offset and the reduced structure (e.g., Fig. 4). The latter can be explained by the coarser resolution of the model than the AVHRR data. MM5 misses to capture some thin cirrus clouds at the end of the simulation period, which can be explained by the coarse vertical resolution at the cirrus level. Note that the effects of the land-cover changes do not reach to these levels (see Section 5). The substantial agreement between simulated and observed low level cloud pattern suggests a good confidence in the capability of MM5 to correctly describe the essential physics of the atmospheric horizontal and vertical motion and the thermodynamic state (including the fate of clouds).

Seventy-seven percent of the predicted precipitation area coincides with that observed; 47% of the predicted precipitation rates are within a factor of 2 of the observations. Nevertheless, averaged over all sites, MM5 tends to appreciably underestimate precipitation. Possible explanations for these discrepancies are initial conditions, the few observations available (76), the unknown data quality (as already discussed in Section 3.2), and the size of the grid increments. An initialization, for instance, of a too dry atmosphere will clearly lead to an underestimation of precipitation. As suggested by Fan and Tilley (2005), moisture assimilation with satellite data certainly may improve predicted precipitation. This, however, is no option for our study, as there are no data to assimilate against a scenario of land-cover change. Given that no parameterization of cumulus convection is used, 5-km horizontal grid spacing may be sufficient for resolving large cumulonimbus, but smaller clouds will be missed. Note that results from a sensitivity study using Grell et al.'s (1991) cumulus parameterization hardly differ from the results discussed here.

Theoretically, a simulation with a smaller grid increment than used here could address the scale issue, but has, among other things, two main shortcomings: (1) the land-cover data are artificially downscaled, i.e., in reality there is no better information, and (2) the lack of observations for comparing model predictions against observations. Nevertheless, several sensitivity studies with model domains covering only one major fire complex, but with smaller grid increments provide results similar to those discussed in the following. These smaller-domain simulations, however, have the deficiencies that (1) there are no, or not enough observation data to evaluate their control run scenarios at all, and (2) they were performed at the lower limit (horizontal increment of 1 km or so) for what MM5 has been designed.

Another aspect may also be important in evaluating precipitation events. One has to consider that predicted precipitation represents a grid-cell average rather than a small isolated intense shower occurring in such a grid-cell. The grid-cell average precipitation is usually

appreciably lower than the precipitation of isolated intense showers occurring within the areas represented by the grid cell. The same will be true even if the horizontal grid increment is finer than in the simulations presented here. If one assumes, for instance, that the simulated precipitation occurs only in about 20% of a grid cell, simulated and observed precipitation amount will match well, on average. By taking into account the latter and the high overlap (>77%) of predicted and observed precipitation area

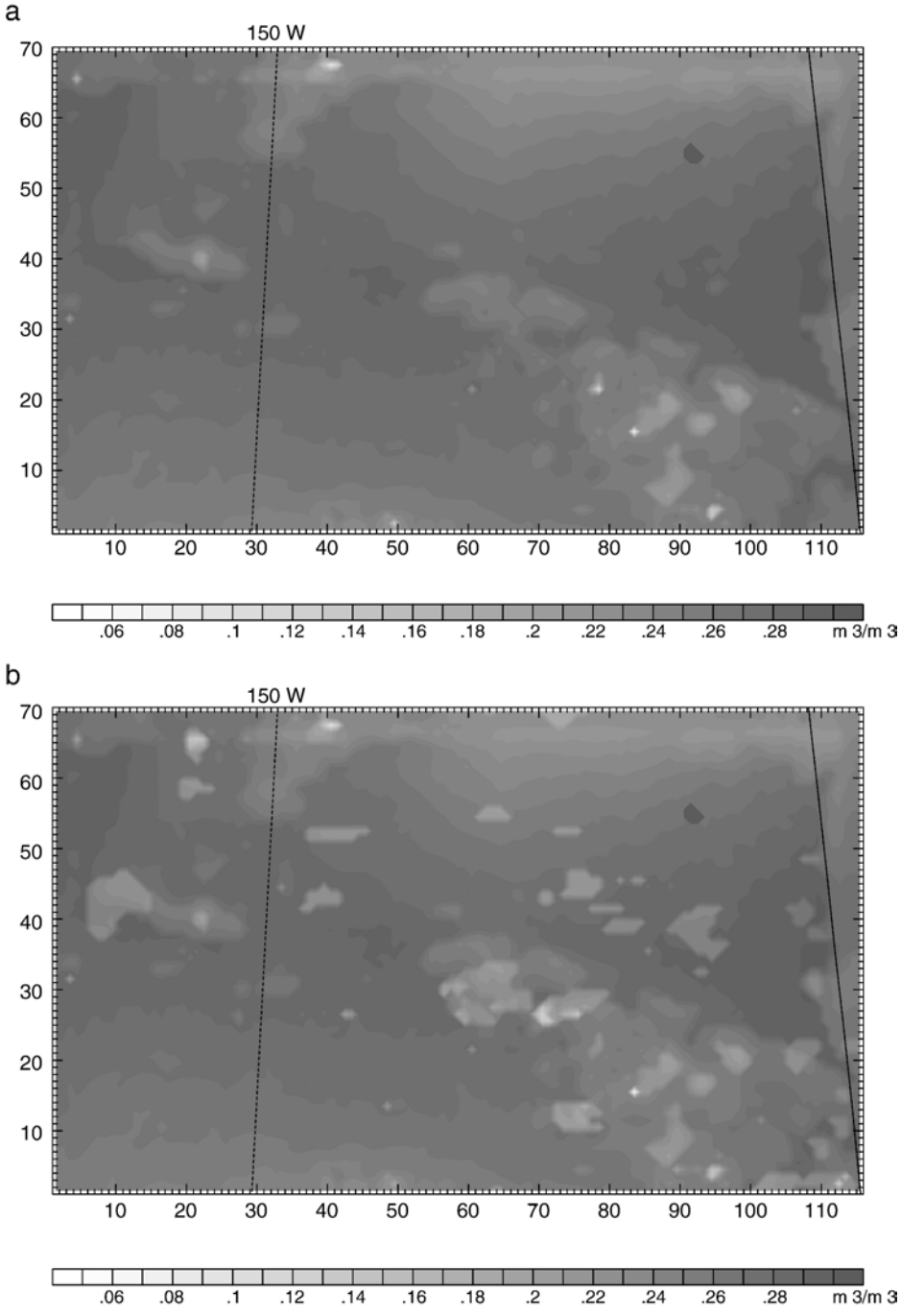

Fig. 5. Soil volumetric water content as obtained for (a) CTR and (b) BRN, and soil temperature as obtained for (c) CTR and (d) BRN at the end of the simulations (after 84 h). The dashed line indicates 150°W longitude.

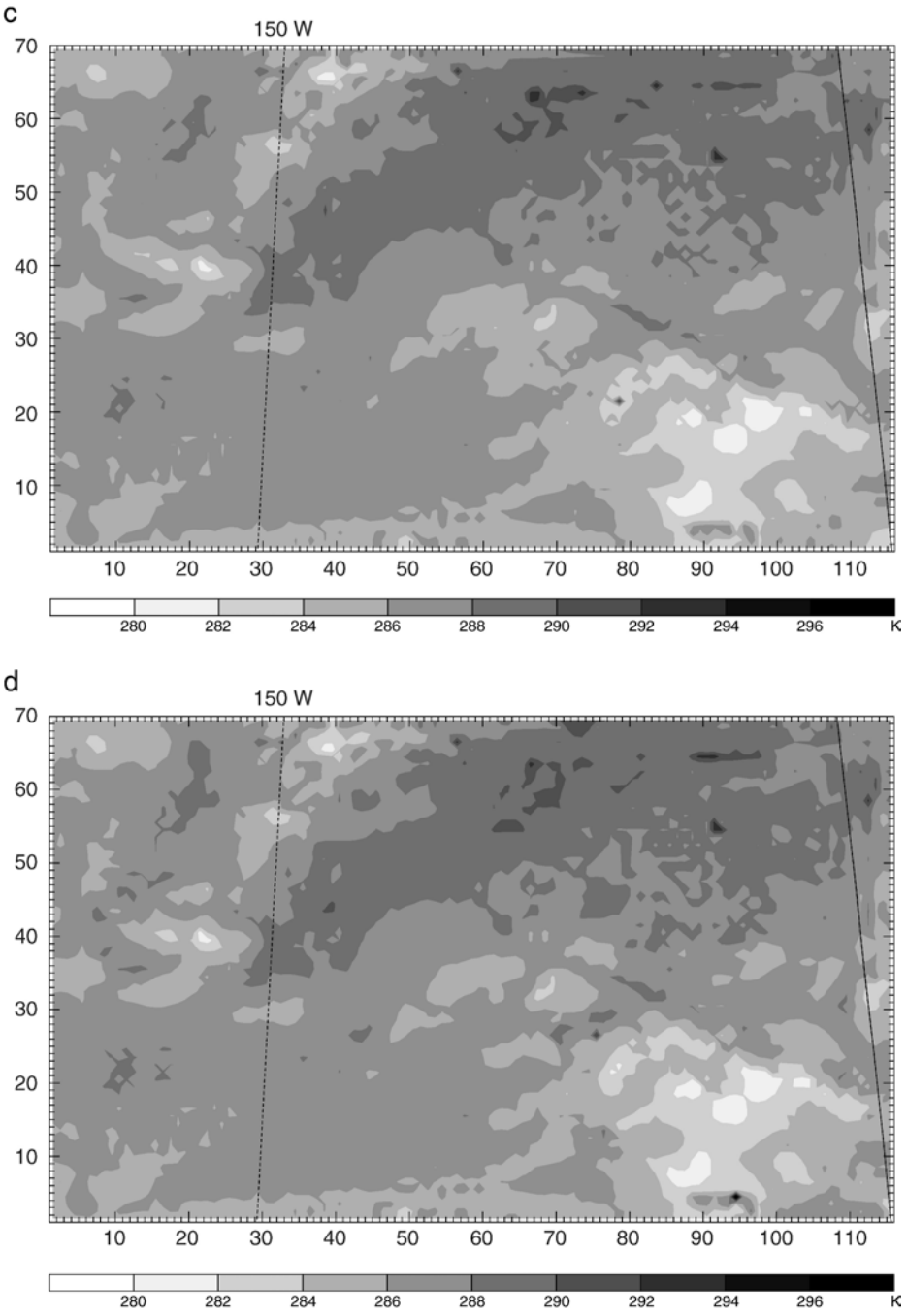

Fig. 5 (*continued*).

as well as the good agreement of simulated and observed cloud distribution (Fig. 4), we conclude that MM5 describes cloud and precipitation processes with an acceptable degree of accuracy. Based on our evaluations, we expect that MM5 will provide reasonable results if the landscape of BRN is assumed. Hence, differences in results of CTR and BRN can be used to examine the impact of wildfire caused land-cover changes on cloud and precipitation formation.

5. Discussion

As described before, the model runs CTR and BRN differ by the land-cover data and related plant and

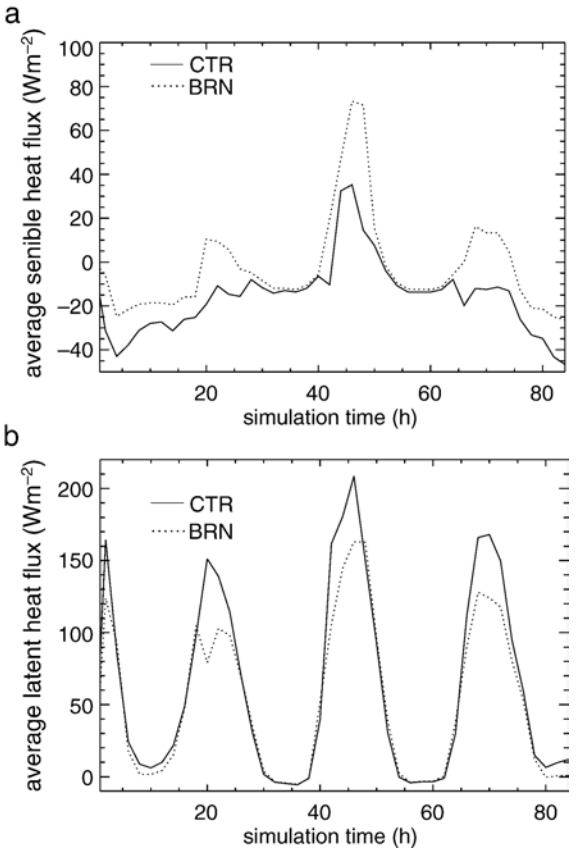

Fig. 6. Temporal development of (a) sensible and (b) latent heat flux over the Boundary/Wolf Creek burnt area for CTR and BRN.

radiative parameters (e.g., vegetation type and fraction, root depth, roughness length, leaf area index (LAI), albedo, emissivity) and initial distribution of soil fields of water, ice, and temperature in the burnt areas. These differences cause sharp horizontal soil temperature and moisture gradients between burnt and adjacent areas that persist throughout the entire simulation (Fig. 5). In most cases, differences in state variables and fluxes increase with increasing size of the (quasi-) coherent burnt area.

5.1. Near-surface fluxes

In HTSVS, the atmospheric fluxes and the soil fluxes of sensible heat and matter are counted positive when directed upward. On the domain-average, net radiation and latent heat fluxes hardly differ between the two simulations. The altered soil and surface conditions of the fire scars, however, lead to primary differences in net radiation, sensible, latent and ground heat flux. Generally, these differences show a diurnal course (e.g., Fig. 6). The altered state variables in response to the land-cover changes also lead to differences outside the burnt areas, defined here as the secondary differences. Secondary differences in net radiation result from altered cloud thickness and/or altered soil volumetric water content and, hence, soil albedo in response to modified precipitation amounts/distribution and latent heat fluxes. For ground heat, sensible, and latent heat fluxes, slight differences occur outside the burnt areas due to the modified air conditions and precipitation distribution that also affect these fluxes.

Over the fire scars, the decreased albedo alters net radiation and the partitioning between sensible, latent and ground heat flux as compared to the pre-fire cover. During the time simulated, some of the soil heat energy is still consumed to thaw the frozen ground in the active layer and, hence, does not contribute to increasing the surface temperature. (From the physical point of view, this soil heat energy, serving for either thawing frozen ground or increasing soil temperature, is referred to as the vertical part of the corresponding flux divergence. If the soil layer under study is so thick that at its deepest level any heat flux vanishes, this vertical part of the flux divergence equals the amount of the penetrating heat flux.) In burnt areas, however, the active layer reaches deeper into the soil than in non-burnt areas (e.g., Fig. 3). During the episode simulated diurnal soil temperature variations did not reach deep enough to cause a diurnal freezing–thawing cycle in burnt areas. At the same depth where the freezing line occurs in the original landscape, the soil is warmer in burnt areas than in the corresponding pre-fire situations. Thus, in burnt areas, energy penetrating into the soil mainly contributes to

Table 4
Area averaged differences Δ = CTR − BRN of selected burnt areas

	Size in MM5 (km^2)	Sensible heat flux (W m^{-2})			Latent heat flux (W m^{-2})		
		CTR	BRN	Δ	CTR	BRN	Δ
Boundary/Wolf Creek	2825	−15.6	−2.3	13.3	61.2	50.8	−10.4
Circle Complex	1600	−10.4	4.2	14.6	71.4	66.0	−5.4
North Dag	1450	−19.2	−6.2	13.0	74.2	69.9	−4.3
Camp Creek	600	−11.8	0.3	12.1	54.9	42.9	−12.0
Burn around x=320 km, y=270 km	350	−6.1	31.0	37.1	84.0	56.4	−27.6
Burn around x=200 km, y=125 km	50	3.7	12.2	8.5	77.5	72.0	−5.5

soil heating and to surface temperature enhancement, thereby increasing the temperature difference at the soil–atmosphere interface. Burnt areas have up to 13.4 K and, averaged over all scars, 2.4 K higher temperatures in the uppermost soil layer than the same area in the pre-fire situation (e.g., Fig. 5).

In burnt areas, the soils are drier with respect to the total soil water content due to water vapor loss during the fire. However, the warmer soil temperatures permit a higher fraction of the total soil water to be in the liquid phase than if there had been no fire. The relatively darker soils of burnt areas are warmer than the same areas in the original landscape. Thus, near-surface air temperature is slightly higher (up to 3 K at local noon) over the burnt than the original areas. In the lee-side regions of burnt areas, air temperatures can be slightly lower (up to 1.6 K) if more rainwater, more cooling from evaporating rainwater and/or melting of precipitating ice occurs in BRN than in CTR. These slight (secondary) differences marginally increase the spatial variance of air temperatures and hardly increase near-surface temperature averaged over the domain (<0.1 K) and burnt area (0.1 K).

Since a difference between the surface temperature and the near-surface air temperature (at a certain level aloft) causes a sensible heat flux, over burnt areas sensible heat fluxes increase by up to 266 W m^{-2} and 16 W m^{-2} on average as compared to the same pre-fire location. During the day sensible heat fluxes are 5 to 25% greater over burnt areas than over the adjacent area or the same place in CTR (e.g., Fig. 6). This result agrees well with the 10 to 20% difference between burnt and adjacent areas found in aircraft measurement in the first years after a fire by Amiro et al. (1999). It differs, of course, from the empirical findings of Liu et al. (2005). This is not surprising because of the different temporal and spatial scales of their observations and our model runs. In areas where clouds occur in BRN but not in CTR, sensible heat fluxes can be up to 102 W m^{-2} lower. Sensible heat fluxes of CTR and BRN differ significantly over burnt areas exceeding 600 km^2 (North Dag, Boundary/Wolf Creek, Camp Creek, Circle Complex). The average difference between the sensible heat fluxes occurring prior to and after the fire is about the same for all burnt areas independent of their size if ≥600 km^2 (e.g., Table 4).

The strength of the latent heat flux mainly depends on strength of the water vapor flux caused by evapotranspiration. Evaporation is caused by the difference between the moisture at the soil surface and that of the near-surface air. Transpiration, on the other hand, is controlled by plant available water in the root zone and plant physiological processes. If the soil is covered by vegetation, the soil water present in the unfrozen root zone of the active layer is available for water uptake by roots. Burnt areas have up to 0.223 m^3 m^{-3} lower soil volumetric liquid water content than their adjacent areas (e.g., Fig. 5). In burnt areas, the average liquid water content of the uppermost soil is 0.052 m^3 m^{-3} lower than at the same place in the original landscape. Volumetric liquid water content of the uppermost soil layer is up to 0.09 m^3 m^{-3} higher in BRN than CTR where precipitation occurred in BRN, but not in CTR.

Since in burnt areas only some short grass (which is only 10% of the original vegetation fraction) exists, the area where water supply to the atmosphere is controlled by plant physiology is reduced and the area controlled by evaporation, which is appreciably affected by soil moisture, is increased. Moreover, in areas where deep-rooting trees burnt, water for transpiration is now taken from soil layers much closer to the surface than in the original landscape because grass has shorter roots than trees (cf. Table 2).

Latent heat fluxes decrease 12 W m^{-2} on average over all burnt areas. In some burnt spots, however, where precipitation occurred in CTR but not BRN, latent heat fluxes increase by up to 295 W m^{-2}. Latent heat fluxes can be appreciably (up to 244 W m^{-2}) lower in areas where no clouds and/or precipitation occur in BRN, but exist in CTR. For mainly forest-surrounded or previously forest covered burnt areas, difference in latent heat fluxes are greater in large than small burnt areas (cf. Fig. 2, Table 4) and the greatest around 1500AST (e.g., Fig. 6).

Latent heat fluxes differ significantly within burnt areas > 800 km^2 or where precipitation and following insolation differ appreciably. Obviously, the burnt area size required to cause significant changes in latent heat flux (800 km^2) is larger than required in the case of the sensible heat flux (600 km^2). The area experiencing significant changes in latent heat fluxes (5075 km^2) is less than that with significant changes in sensible heat fluxes (8625 km^2).

On domain-average, Bowen ratio and its variance only slightly increase in BRN as compared to CTR. During the day, on average, the burnt areas have about 25 to 45% higher Bowen ratio values than the corresponding pre-fire locations. This finding broadly agrees with the about 50% reported by Amiro et al. (1999).

5.2. Clouds

Moist static energy increases (by up to 5125 J) over the burnt areas, and slightly decreases in their leeside

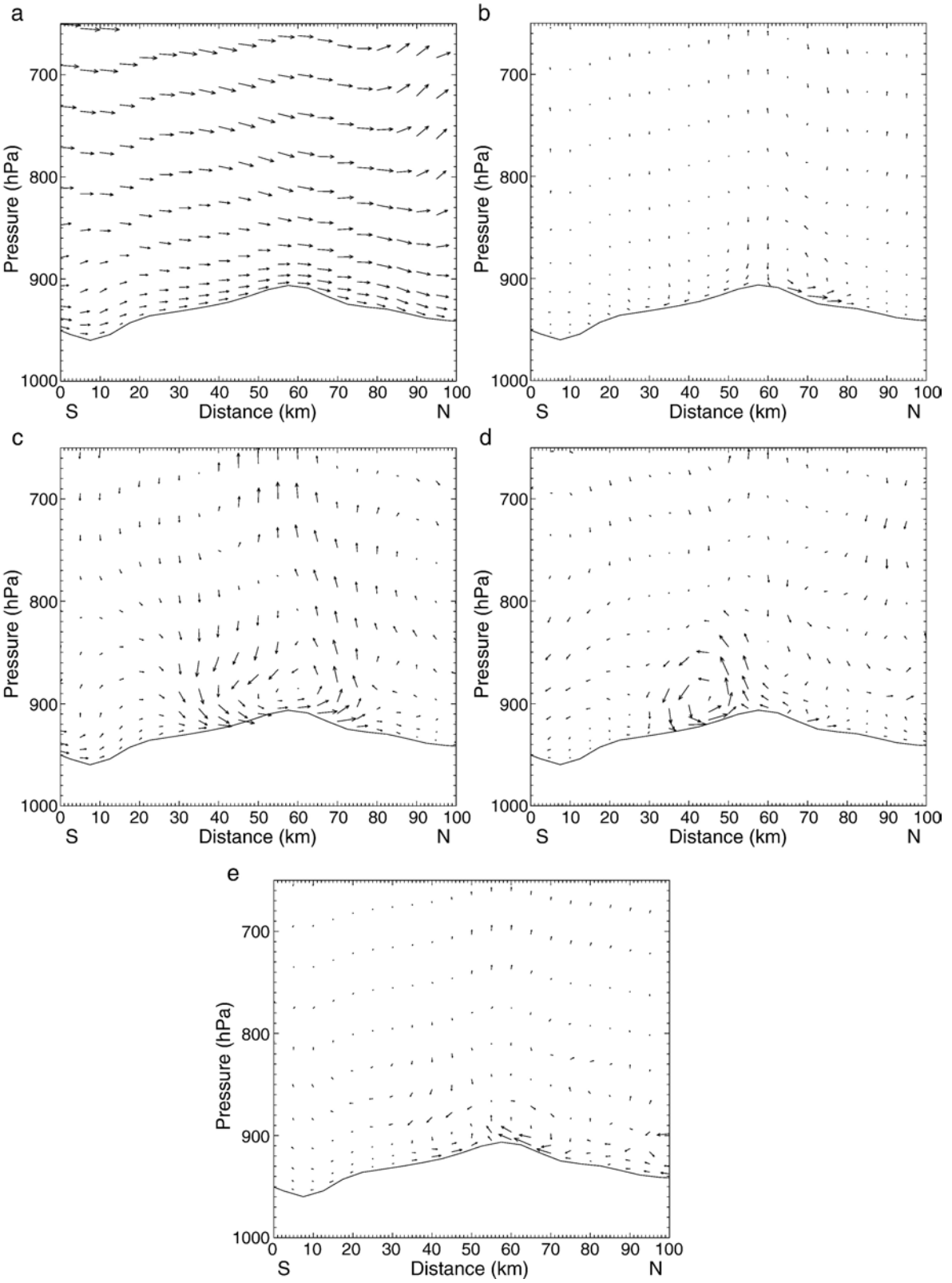
a
b
c
d
e
Pressure (hPa)
700
800
900
1000
0 10 20 30 40 50 60 70 80 90 100
S
Distance (km)
N

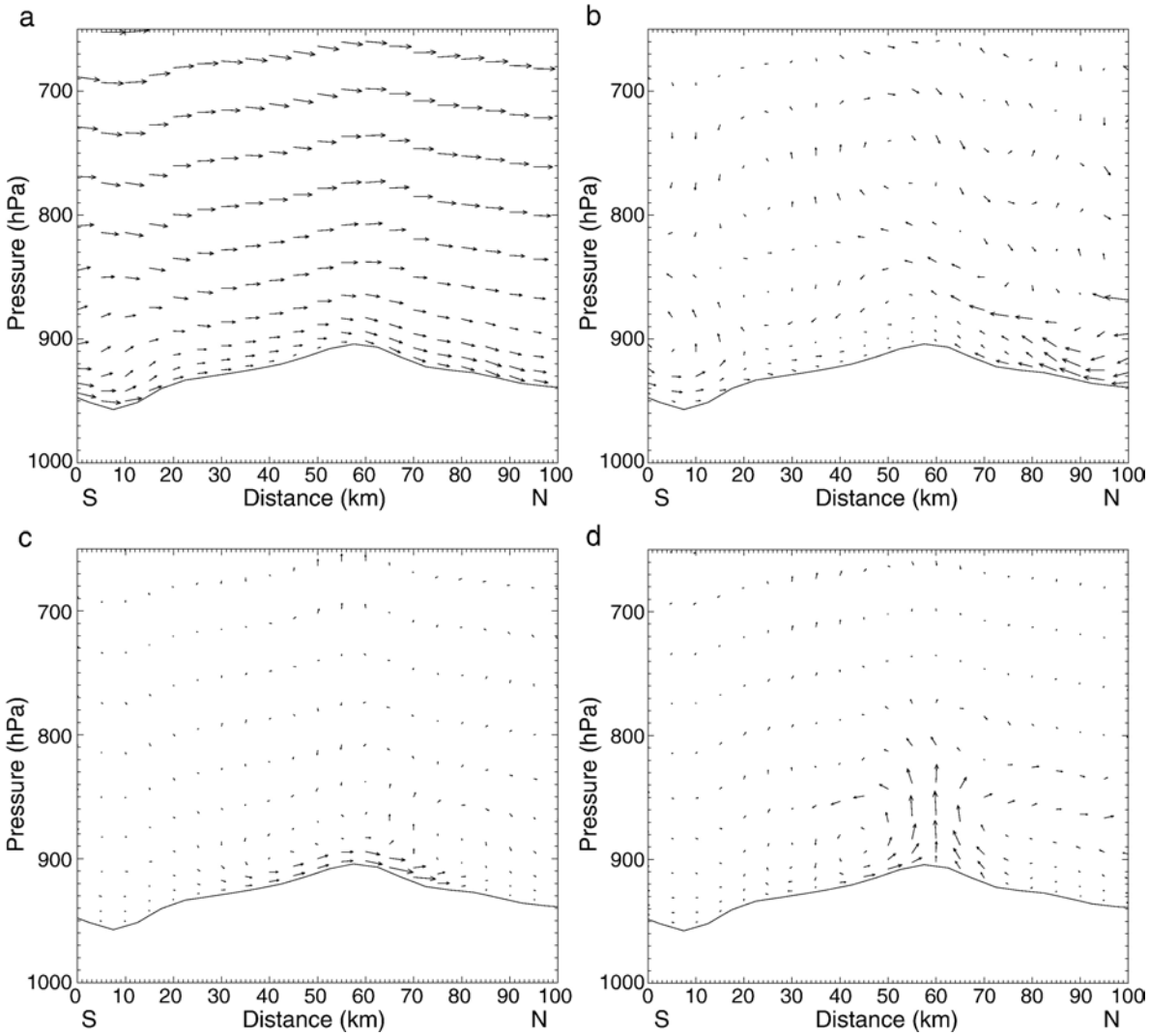

Fig. 8. Like Fig. 7, but for (a) wind vectors on July 22 1400UT (0500AST), max. horizontal and vertical vector component 7.3 m/s, 89 Pa/s. Differences of wind vectors BRN-CTR (b) on July 22 1400UT (0500AST), max. horizontal and vertical vector component 0.4 m/s, 7 Pa/s, (c) on July 22 1800UT (0900AST), max. horizontal and vertical vector component 0.4 m/s, 5 Pa/s, and (d) on July 23 0000UT (July 22 1500AST), max. horizontal and vertical vector component 0.5 m/s, 32 Pa/s.

regions (by up to 300 J). The convective inhibition (CIN), i.e., the energy per unit mass (see Appendix A) needed to lift an air parcel (unit mass) vertically and pseudo-adiabatically from its originating level (OL) to its level of free convection (LFC), represents a static stability barrier. As shown in Appendix A, this barrier can be related to a minimum of the vertical velocity at the OL by

$$w_{\mathrm{OL,min}} = +\sqrt{-2\mathrm{CIN}} \tag{5}$$

Thus, the condition $w_{\mathrm{OL}} \geq w_{\mathrm{OL,min}}$ must be fulfilled to guarantee the occurrence of free convection. Based on

Fig. 7. South–north cross section over the Boundary/Wolf Creek area. (a) Wind vectors as obtained by CTR on July 20 1400UT (0500AST), max. horizontal and vertical vector component 7.3 m/s, 89 Pa/s. Differences of wind vectors BRN-CTR (b) on July 20 1400UT (0500AST), max. horizontal and vertical vector component 0.5 m/s, 5 Pa/s, (c) on July 20 2000UT (1100AST), max. horizontal and vertical vector component 0.2 m/s, 8 Pa/s, (d) on July 21 0200UT (July 20 1700AST), max. horizontal and vertical vector component 0.3 m/s, 9 Pa/s, and (e) July 21 0600UT (July 20 2100AST), max. horizontal and vertical vector component 0.4 m/s, 8 Pa/s. Note that the vector field remains nearly constant with time for CTR (therefore other times are not shown). The burnt area is located between 25 km and 75 km.

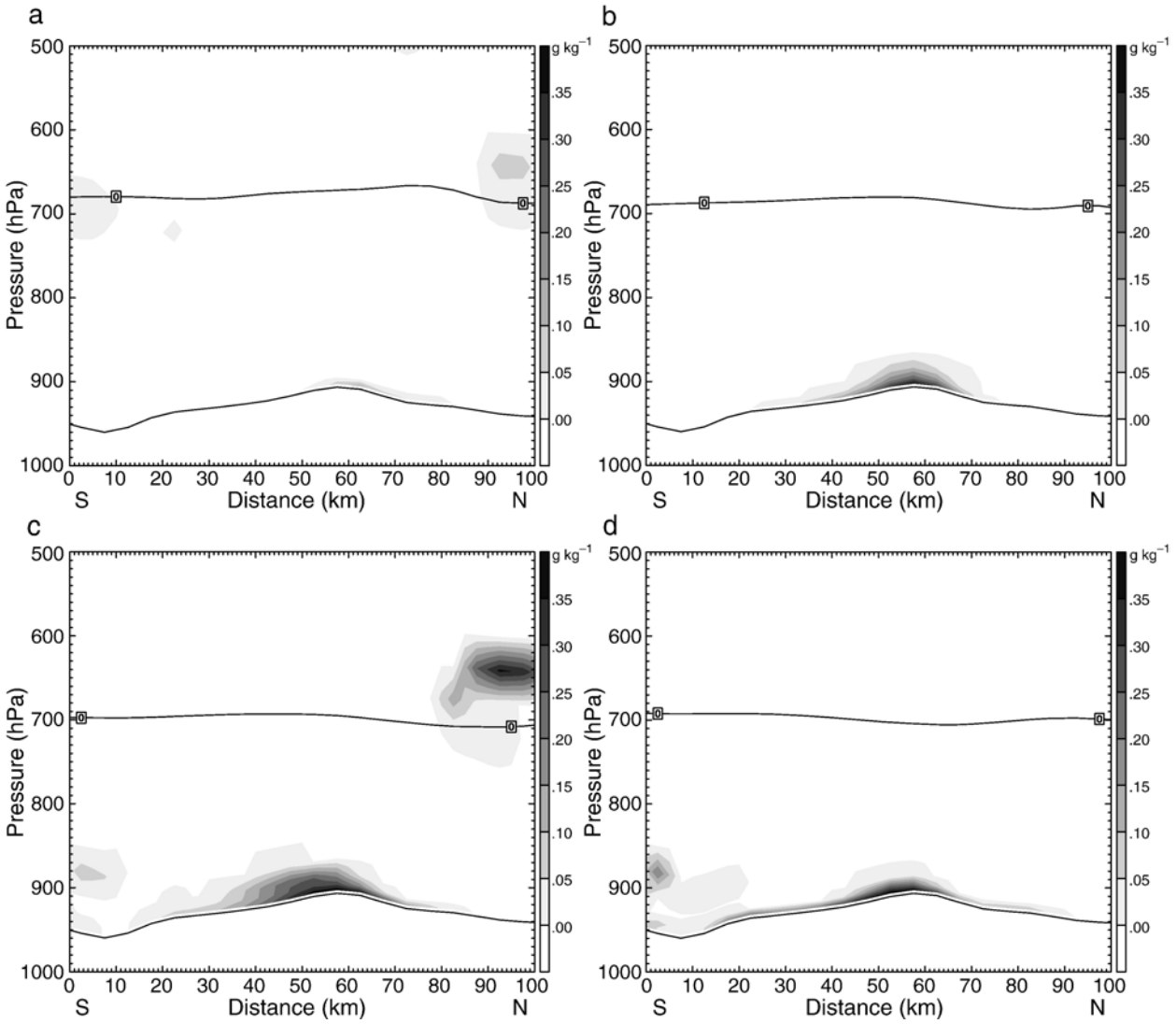

Fig. 9. South–north cross section over the Boundary/Wolf Creek area. Sum of cloud-water and ice mixing ratio as obtained by CTR (a) on July 20 1400UT (0500AST), (b) on July 20 2000UT (1100AST), (c) on July 21 0200UT (July 20 1700AST), (d) on July 21 0600UT (July 20 2100AST). Differences BRN-CTR of sum of cloud-water and ice mixing ratio (e) on July 20 1400UT (0500AST), (f) on July 20 2000UT (1100AST), (g) on July 21 0200UT (July 20 1700AST), and (h) on July 21 0600UT (July 20 2100AST). The solid line is the 0 °C-isotherm. Note that liquid water is super-cooled at temperatures below 0 °C and may lead to aircraft icing. Contour line spacing is 0.1 g/kg. Negative values are dotted. The burnt area is located between 25 km and 75 km.

Eq. (5), one can show that small changes in vertical motions can have great effects on the ability to initiate convection. As pointed out, for instance, by Chase et al. (1999), a 5% increase in the vertical velocity from 0.100 to 0.105 m/s enhances the static stability barrier that a parcel can overcome by 10% and thus raises the potential for convection.

On the domain-average, vertical wind speed hardly differs between BRN and CTR. However, vertical motions simulated by CTR and BRN differ notably over and in the lee-side regions of burnt areas > 600 km^2 and are the greatest in the lower ABL (e.g., Figs. 7 and 8). Over burnt areas of this size, differences in vertical motions start marginally around sunrise and build up to a non-classical mesoscale circulation-type (Segal and Arritt, 1992) upward motion about 2 h after local noon (1500AST; Figs. 7 and 8). Once insolation decreases due to the lower position of the sun in the sky and increased cloud formation in the late afternoon, the upward motion weakens and differences in vertical motions nearly vanish after sunset. Differences start growing again after sunrise. This pattern can be found in

a more or less distinct manner for all days of the simulation episode (e.g., Figs. 7 and 8). In the lee-side regions of burnt areas where precipitation of BRN exceeds that of CTR, downward vertical motions are stronger in the former than the latter. Nevertheless, differences are only significant over and in the lee-side regions of burnt areas exceeding a size of 1600 km^2 like the Boundary/Wolf Creek and Circle Complex areas.

If moist air reaches the lifting condensation level, clouds will form. The altered surface fluxes and, in response, the altered state variables are the most effective path to affect the ABL and the fate of clouds. Over burnt areas, near-surface temperatures are higher (up to 3 K and 0.1 K on average over all burnt areas) than at the same place in CTR. In BRN, water vapor mixing ratios vary from 2.73 g/kg less, to 3.93 g/kg larger than those at the same locations in CTR due to differences in evaporation of rainwater/ice in areas with downward directed motion and the position of downward directed motion. Averaged over the burnt areas and the domain, near-surface water vapor mixing ratios decrease insignificantly by 0.022 g/kg and 0.001 g/kg, respectively. This finding indicates marginally drier conditions for BRN than for CTR.

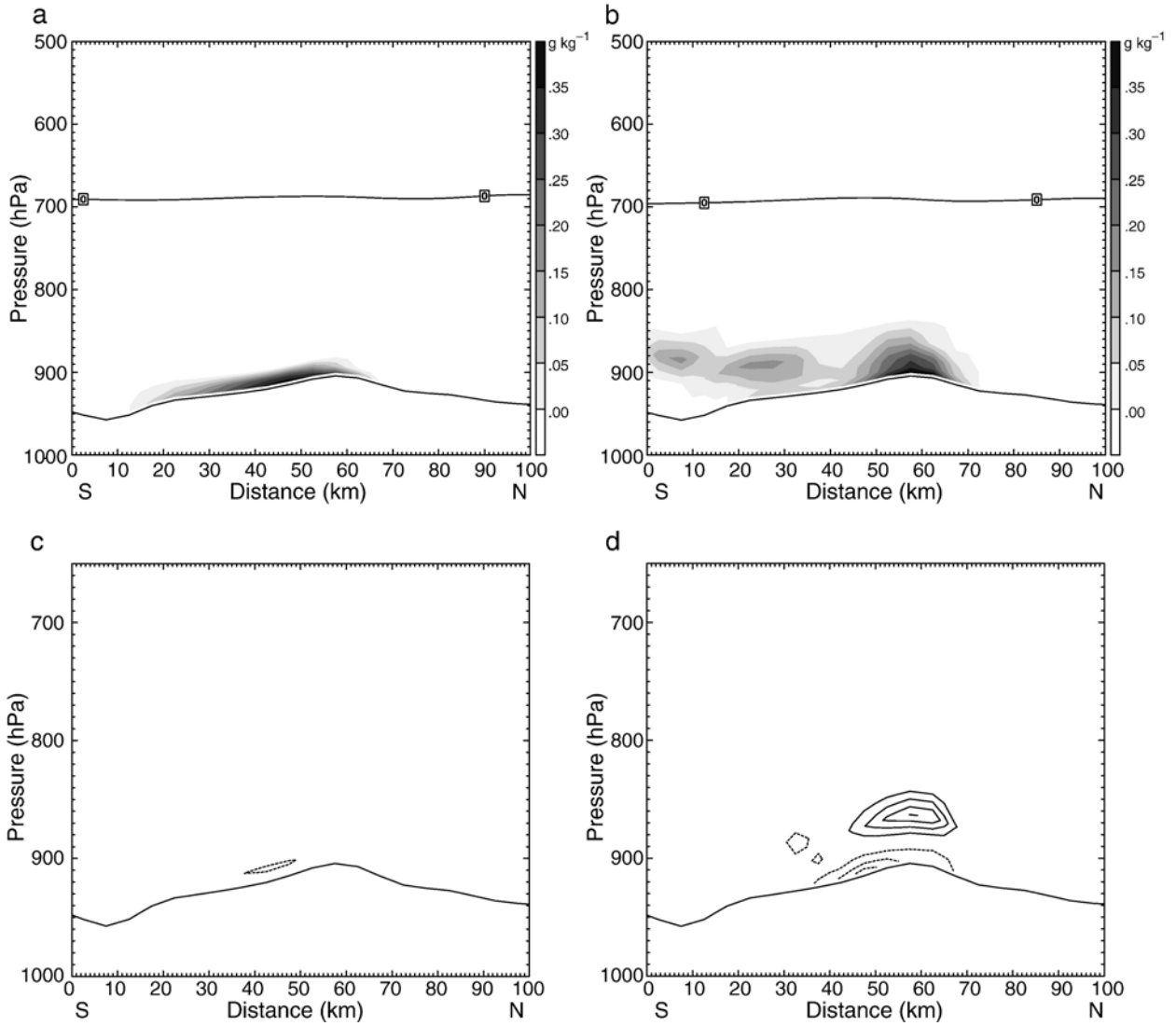

Fig. 10. Like Fig. 9, but for the sum of cloud-water and ice mixing ratio (a) on July 22 1800UT (0900AST), (b) on July 23 0000UT (July 22 1500AST). Differences BRN-CTR of sum of cloud-water and ice mixing ratio (c) on July 22 1800UT (0900AST), and (d) on July 23 0000UT (July 22 1500AST). Note that there are no clouds in both simulations on July 22 1400UT (therefore not shown).

The appreciably decreased latent heat fluxes and significantly increased sensible heat fluxes over burnt areas > 600 km^2 force an increased vertical transport of moist air in BRN as compared to CTR and strongly affect cloud formation (e.g., Figs. 9 and 10). These differences in cloud conditions build up in the diurnal course from marginal around sunrise to appreciable differences in cloud (cloud-water plus cloud ice) mixing ratios about 2 h after local noon. Maximum differences in hydrometeor (rainwater, graupel and snow) mixing ratios occur with a slight temporal offset. As the upward transport weakens, differences in cloud and hydrometeor mixing ratios diminish (e.g., Figs. 7–10). Like for vertical motions, the differences in cloud and hydrometeor mixing ratios can be detected for all days of the episode (e.g., Figs. 9 and 10).

The greatest changes in cloud and hydrometeor mixing ratios occur in the ABL in the leeward part of burnt areas > 600 km^2 and their leeside. As compared to CTR, cloud-water, rainwater, and ice mixing ratios are sometimes locally enhanced (reduced) by up to 0.55, 0.08 and 0.03 g/kg (0.5, 0.09 and 0.04 g/kg) in BRN. Thus, also the pattern of areas with great amounts of super-cooled water and, hence, the risk of aircraft icing differ in the original and fire-changed landscape. The total number of grid cells with significant differences is smaller for solid (ice 278, graupel 1490) than liquid (cloud-water 4469, rainwater 5960) cloud and precipitating particles. While significant changes in cloud-water, rainwater and graupel mixing ratios occur downwind of burnt areas exceeding 600 km^2 (Camp Creek, Boundary/Wolf Creek, Circle Complex, North Dag), changes in ice mixing ratios are randomly distributed.

As mentioned in the introduction, lightning activity depends on charge separation and transfer, which can be caused by graupel and updraft formation. Thus, differences in the formation of graupel between BRN and CTR are of particular interest. Generally, graupel occurs earlier and lasts longer, but in lower mixing ratios in the post-fire landscape than in the original landscape. Locally graupel mixing ratios differ by up to ±0.03 g/kg between CTR and BRN with smaller differences in the lower ABL. In the upper part of the clouds, graupel mixing ratios decrease significantly over and in the leeside regions of all burnt areas > 600 km^2 (Camp Creek, North Dag, Boundary/Wolf Creek, Circle Complex) between 1700 and 0100AST. An area of increased graupel mixing ratio follows downwind. This area, however, is smaller than the preceding area of decreased graupel mixing ratios. Since graupel formation can lead to the occurrence of lightning, one has to expect that recently burnt areas > 600 km^2 may reduce lightning

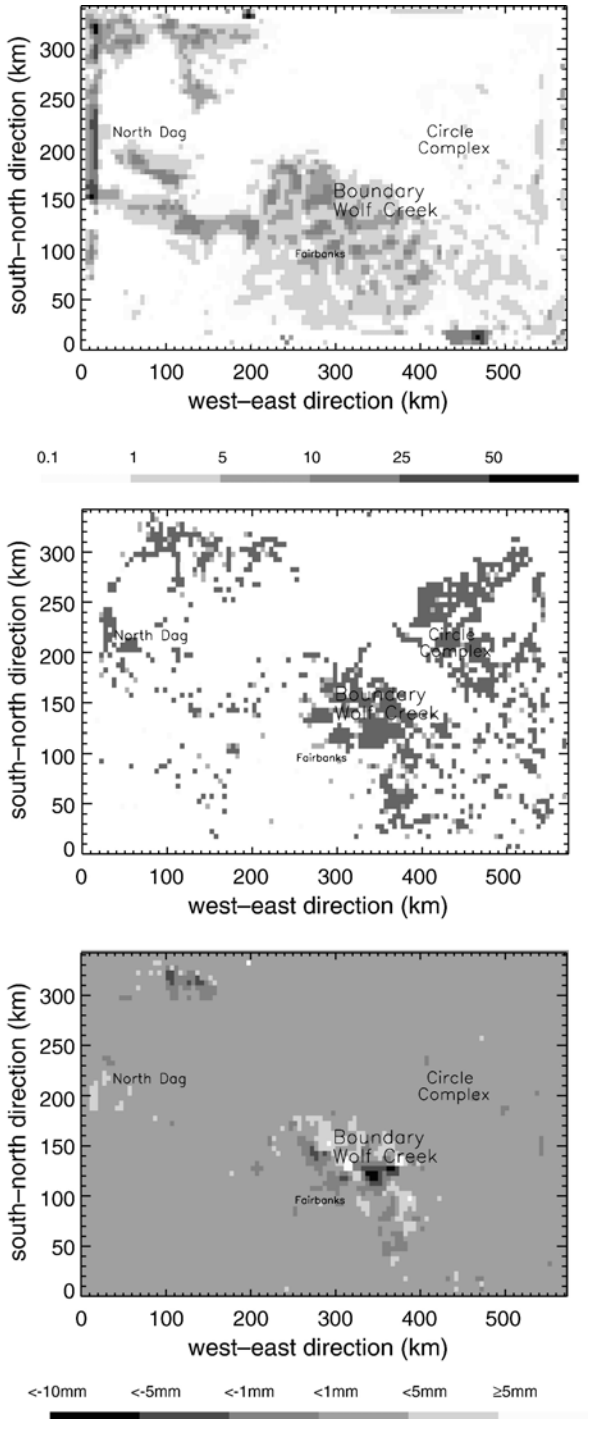

Fig. 11. (a) 84 h-accumulated precipitation as obtained by CTR, (b) areas of significant changes in 84 h-accumulated precipitation (in (a) and (b) gray shades light to dark gray indicate significance at the 90, 95 and 99% confidence level according to an F-variance test), and (c) differences in 84 h-accumulated precipitation CTR-BRN.

frequency, but enlarge the time period during which lightning may occur.

5.3. Precipitation

The described changes in hydrometeor mixing ratios lead to shifts in the temporal and spatial distribution, accumulated amount and rate of precipitation. In the lee-side regions of burnt areas > 600 km^2 (North Dag, Boundary/Wolf Creek, Circle Complex, Camp Creek), daily precipitation and 84 h-accumulated precipitation are up to 13.7 mm and 15.1 mm higher than at the same locations in the original landscape (e.g., Fig. 11). Farther downwind of burnt areas > 600 km^2, daily and 84 h-accumulated precipitation are up to 8.8 and 9.3 mm less in BRN than in CTR because more water was removed from the atmosphere farther upwind in the former than the latter. Maximum 84 h-accumulated precipitation of CTR and BRN amounts to 78 mm and 68.2 mm, respectively, but precipitation occurs at different places for CTR and BRN (Fig. 11).

A total of 31,625 km^2 shows significant differences in precipitation in the lee of burnt areas > 600 km^2 (North Dag, Boundary/Wolf Creek, Camp Creek, Circle Complex), i.e., 15% of the model domain experiences significant precipitation changes (Fig. 11). The local maximum precipitation rate in BRN exceeds that of CTR by more than 12%. This means that the risk of local flash floods increases in the fire-changed landscape as compared to the original landscape.

In BRN, domain-averaged precipitation is up to 58% higher in the first 24 h and about 7% less afterwards than in CTR. The 84 h-accumulated domain-averaged precipitation decreases marginally (0.1 mm) in BRN as compared to CTR. This means that the burnt areas cause a shift towards drier conditions (lower total soil volumetric water content, less precipitation and water vapor on the domain average) for weather conditions with strong local recycling of water over several days like the one in our case study.

6. Mechanism

The study showed that burnt areas > 600 km^2 may affect cloud formation and enhance precipitation in their immediate downwind (Figs. 9–11), while establishing a shift towards a marginally drier regime on domain-average. The mechanism leading to this result can be explained as follows: A burnt area reflects less solar radiation to the atmosphere and accumulates more heat than did the former vegetation. The heat stored in the soil during the fire (Fig. 3) and the fact that soil heat flux does not serve to thaw frozen ground also contribute to a warmer surface. Thus, burnt areas have enhanced surface temperatures and, if > 600 km^2, locally significantly higher sensible heat fluxes. In principle, these changes contribute to a slightly warmer ABL over the burnt areas. As compared to the same place in the original landscape, evapotranspiration and hence latent heat fluxes significantly decrease over burnt areas > 800 km^2 because of the change in the soil moisture regime and vegetation type and coverage. The little vegetation present for transpiration in BRN takes the water from the unfrozen upper soil, while in CTR the vegetation fraction is larger and roots of trees can also take up plant available water from deeper layers. The heating generated by the warmer surface increases the vertical wind component and upward transport of air in the ABL notably over burnt areas > 600 km^2. However, burnt areas must exceed 1600 km^2 for the changes to be significant. For continuity reasons this air is replaced by moist air from the adjacent vegetation covered areas. This means that burnt areas > 600 km^2 establish an effective mechanism to lift moist air (e.g., Figs. 7 and 8) from the burnt environment upwards (Fig. 12). As the air is slightly warmer, condensation occurs at higher levels than air lifted in non-burnt areas or the same locations in the original landscape (e.g., Figs. 9 and 10). Due to the enhanced moist static energy cloud tops reach (up to 500 m) higher into the mid-troposphere in the leeside regions of burnt areas than in adjacent areas or the same place in the original landscape. Thus, in BRN, air is cooler in the upper part of the clouds than in CTR where clouds do not reach so high. Thus, more rainwater is built via the cold path of precipitation formation (water vapor deposition onto ice nuclei and ice particles, growth during sedimentation by riming and later melting of ice particles at temperatures higher than the freezing point) in the post- than pre-fire landscape. Since the saturation pressure of ice is less than that of water, this shift towards a higher preference for the cold path leads to more efficient use of water vapor for cloud- and precipitation formation processes and significant changes of cloud-water and ice mixing ratios and precipitation (e.g., Figs. 9–11).

Furthermore, follow-up changes result from the interacting cloud microphysics dynamics as the falling hydrometeors, evaporative cooling and cooling by melting can turn slightly upward motions into downward motion. This effect explains the decrease in cloudiness found behind the area of increased cloud and hydrometeor mixing ratios and precipitation in the leeside regions of burnt areas > 600 km^2 (Figs. 9–11).

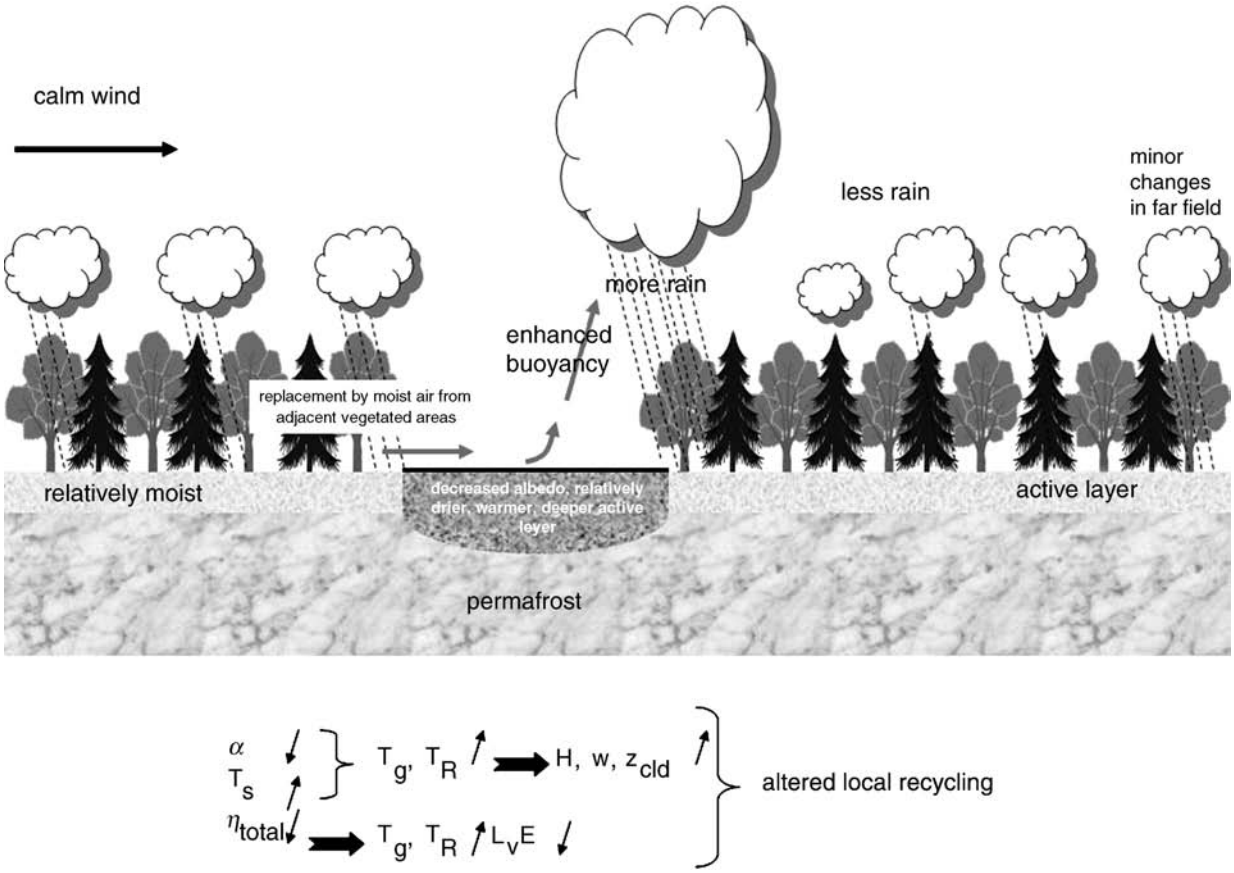

Fig. 12. Schematic view of mechanism for altered features.

Overall, the changes reduce the domain-averaged accumulated precipitation, but intensify precipitation downwind of burnt areas > 600 km^2.

The altered distributions and intensities of precipitation yield slight differences in soil volumetric water content in the lee side of burnt areas (Fig. 5) that again modify evapotranspiration even far away from the fire scars. This impact on the "far-field" will propagate as long as precipitation formation mainly results from local recycling of previous precipitation. Another "far-field" effect results from the higher reaching clouds.

7. Conclusions

Numerical experiments were performed with the PennState/NCAR Mesoscale Model MM5 alternatively assuming the landscape prior to and after the 2004 fire season in Interior Alaska, mainly to examine the impact of wildfire induced land-cover changes on clouds and precipitation. Burnt areas were realized by changing (1) the radiative (albedo, emissivity), (2) vegetative (vegetation type, fraction, LAI, stomatal resistance), (3) thermal (soil heating, thawing of permafrost), and (4) hydrological (water loss due to the fire, reduced transpiration) surface characteristics. As the evaluation of the control run indicated a good confidence in the capability of MM5 to predict the cloud and precipitation formation processes rather well, we argued that MM5 can also be used for examining the impact of wildfire induced land-cover changes on the fate of clouds and precipitation.

Compared to the control simulation, burnt areas cause a shift in the partitioning of net radiation between ground, sensible and latent heat fluxes. The altered surface forcing affects the state variables, vertical motion, and the paths of cloud and precipitation formation. Despite the fact that in relatively small burnt areas sensible heat fluxes prior to and after the fire may differ even more than for comparable larger burnt areas, a burnt area > 600 km^2 is required to heat the air long enough to initiate a notable upward motion at its downwind edge, causing significant (at the 90% or even higher confidence level according to an *F*-

variance test) local changes in the clouds and hydrometeors as well as in precipitation. The change in sensible heat fluxes over burnt areas > 600 km^2 establishes vertical motion as found in the upward branch of so-called non-classical mesoscale circulations (Segal and Arritt, 1992). Sensible and latent heat fluxes and vertical wind velocity change significantly over burnt areas > 600, 800 and 1600 km^2, respectively. The enhanced upward transport of heat and moisture shifts the cloud and precipitation formation process towards the cold path. Due to the lower saturation vapor pressure over ice than water precipitation is formed more efficiently increasing precipitation in the leeside of the burnt area. As more water vapor was removed from the atmosphere in the upwind, less precipitation occurred downwind of these areas of enhanced cloud and precipitation formation. This means that wildfire induced land-cover changes can significantly influence the temporal and spatial precipitation distribution without changing the landscape-average precipitation. The local increases in precipitation rates of more than 12%, however, mean an enhanced risk of flooding by creeks in landscapes with recently burnt areas > 600 km^2. Consequently, despite on the domain average the differences are marginal they become quite noticeable on the local scale and are of interest for flash flood forecasts.

The greatest changes in super-cooled cloud-water and rainwater mixing ratios occur in the ABL at the flight altitude of small airplanes, and hence may pose a threat to air traffic. Unfortunately, air service is of critical importance for Alaska's economy (supply of goods, fuel, mail, medical care, etc. to remote villages) and tourism, since so much of the state is not accessible by road and the land area is vast. Therefore, future studies should examine the impact of wildfire caused land-cover changes on icing frequency in the long-term.

Acknowledgements

We thank M. Shulski, G. Wendler, R. Smith and the anonymous reviewers for fruitful discussion, K. Engle from the Geographic Information Network of Alaska (GINA) for support with the satellite data processing, C. O'Connor for editing, and NSF for support under Contract ATM0232198.

Appendix A. CIN and CAPE

Assuming that the environment is hydrostatically balanced and the pressure acting on an air parcel (of unit mass) lifted vertically and pseudo-adiabatically is always adjusted to that of the environment, the vertical acceleration of this air parcel can be expressed by (e.g., Haltiner and Martin, 1957)

$$\frac{\mathrm{d}w}{\mathrm{d}t} = \frac{g}{T_\mathrm{v}}\left(T_\mathrm{v,p} - T_\mathrm{v}\right) \tag{A1}$$

Here, w is the vertical velocity of the air parcel, g is the acceleration due to gravity, and $T_\mathrm{v,p}$ and T_v are the virtual temperatures of the air parcel and environment, respectively. Multiplying both sides of this equation by the differential of the height, dz, and applying some algebra yield

$$\begin{aligned}\mathrm{d}z\frac{\mathrm{d}w}{\mathrm{d}t} &= \frac{\mathrm{d}z}{\mathrm{d}t}\mathrm{d}w = w\ \mathrm{d}w = \frac{\mathrm{d}}{\mathrm{d}t}\frac{w^2}{2} \\ &= \frac{g}{T_\mathrm{v}}\left(T_\mathrm{v,p} - T_\mathrm{v}\right)\mathrm{d}z\end{aligned} \tag{A2}$$

Expressing dz by the hydrostatic equation

$$\mathrm{d}z = -\frac{1}{\rho g}\mathrm{d}p = -\frac{R_\mathrm{d}T_\mathrm{v}}{g}\frac{\mathrm{d}p}{p} \tag{A3}$$

provides

$$\frac{\mathrm{d}}{\mathrm{d}t}\left(\frac{w^2}{2}\right) = -R_\mathrm{d}\left(T_\mathrm{v,p} - T_\mathrm{v}\right)\mathrm{d}(\ln p) \tag{A4}$$

Here, R_d and p are the gas constant for dry air and air pressure, respectively. Integration from the originating pressure level, p_OL, to the pressure level of free convection, p_LFC, where the two temperature curves intersect, yields the kinetic energy change per unit mass for the moving parcel (e.g., Haltiner and Martin, 1957)

$$\begin{aligned}w_\mathrm{LFC}^2 = w_\mathrm{OL}^2 &= -2\int_{p_\mathrm{OL}}^{p_\mathrm{LFC}} R_\mathrm{d}\left(T_\mathrm{v,p} - T_\mathrm{v}\right)d(\ln p) \\ &= 2\int_{p_\mathrm{LFC}}^{p_\mathrm{OL}} R_\mathrm{d}\left(T_\mathrm{v,p} - T_\mathrm{v}\right)d(\ln p)\end{aligned} \tag{A5}$$

If, in the region between p_OL and p_FLC, the temperature condition $T_\mathrm{v,p} \le T_\mathrm{v}$ is fulfilled, one will obtain

$$\int_{p_\mathrm{LFC}}^{p_\mathrm{OL}} R_\mathrm{d}\left(T_\mathrm{v,p} - T_\mathrm{v}\right)d(\ln p) \le 0 \tag{A6}$$

i.e., there is a "negative energy" region usually called the convective inhibition (CIN). It represents a stability barrier which an air parcel has to overcome to reach the level of free convection. This means that a certain amount of energy per unit mass is required to lift an air parcel vertically and pseudo-adiabatically from its

originating level to its level of free convection. According to Eq. (A5), this fact can be expressed by

$$w_{\mathrm{LFC}}^2 = w_{\mathrm{OL}}^2 + 2\mathrm{CIN} \geq 0 \tag{A7}$$

i.e., $w_{\mathrm{OL}}^2 \geq 2$ CIN must be fulfilled to guarantee the occurrence of free convection. The required minimum of w_{OL} is given by

$$w_{\mathrm{OL,min}} = +\sqrt{-2\mathrm{CIN}} \tag{A8}$$

Aloft at the level of free convection, the temperature condition $T_{\mathrm{v,p}} > T_{\mathrm{v}}$ is fulfilled (until the two temperature curves intersect again) so that

$$\int_{p_{\mathrm{LFC}}}^{p_{\mathrm{OL}}} R_{\mathrm{d}}(T_{\mathrm{v,p}} - T_{\mathrm{v}})\, d(\ln p) > 0 \tag{A9}$$

This "positive energy" region is called the convective available potential energy (CAPE). It represents the amount of buoyant energy available to accelerate an air parcel vertically.

References

Amiro, B.D., MacPherson, J.I., Desjardin, R.L., 1999. BOREAS flight measurements of forest-fire effects on carbon dioxide and energy fluxes. Agric. For. Meteorol. 96, 199–208.

Anthes, R.A., 1983. Regional models of the atmosphere in middle latitudes. Mon. Weather Rev. 111, 1306–1335.

Anthes, R.A., 1984. Enhancement of convectionale precipitation by mesoscale variations in vegetative covering in semiarid regions. J. Clim. Appl. Meteorol. 23, 541–554.

Anthes, R.A., Kuo, Y.H., Hsie, E.Y., Low-Nam, S., Bettge, T.W., 1989. Estimation of skill and uncertainty in regional numerical models. Quart. J. R. Meteorol. Soc. 111, 763–806.

Avissar, R., Liu, Y., 1996. Three-dimensional numerical study of shallow convective clouds and precipitation induced by land surface forcing. J. Geophys. Res. 101D3, 7499–7518.

Berdeklis, P., List, R., 2001. The ice crystal–graupel collision charging mechanism of thunderstorm electrification. J. Atmos. Sci. 58, 2751–2770.

Beringer, J., Hutley, L.B., Tapper, N.J., Coutts, A., Kerley, A., O'Grady, A.P., 2003. Fire impacts on surface heat, moisture and carbon fluxes from a tropical savanna in northern Australia. Int. J. Wildland Fire 12, 333–340.

Bougeault, P., Bret, B., Lacarrère, P., Noilhan, P., 1991. An experiment with an advanced surface parameterization in a mesobeta-scale model. II. The June 1986 simulation. Mon. Weather Rev. 119, 2374–2393.

Bromwich, D.H., Cassano, J.J., Klein, T., Hines, K.M., Steffen, K., Box, J.E., 2001. Mesoscale modeling of katabatic winds over Greenland with the polar MM5. Mon. Weather Rev. 129, 2290–2309.

Cahoon Jr., D.R., Stocks, B.J., Levine, J.S., Cofer III, W.R., Pierson, J. M., 1994. Satellite analysis of the severe 1987 forest fires in northern China and southeastern Siberia. J. Geophys. Res. 99D, 18627–18638.

Cassano, J.J., Box, J.E., Bromwich, D.H., Li, L., Steffen, K., 2001. Evaluation of Polar MM5 simulations of Greenland's atmospheric circulation. J. Geophys. Res. 106, 33867–33890.

Chambers, S.D., Beringer, J., Randerson, J.T., Chapin III, F.S., 2005. Fire effects on net radiation and energy partitioning: contrasting responses of tundra and boreal ecosystems. J. Geophys. Res. 110, D09106, doi:10.1029/2004JD005299.

Chang, J.T., Wetzel, P.J., 1991. Effects of spatial variations of soil moisture and vegetation on the evolution of a prestorm environment: a case study. Mon. Weather Rev. 119, 1368–1390.

Changnon, S.A., 1980. Evidence of urban and lake influences on precipitation in the Chicago area. J. Appl. Meteorol. 10, 1137–1159.

Chase, T.N., Pielke Sr., R.A., Kittel, T.G.F., Baron, J.S., Strohlgren, T.J., 1999. Potential impacts on Colorado Rocky Mountain weather due to land use changes on the adjacent Great Plains. J. Geophys. Res. 104D, 16673–16690.

Chen, F., Dudhia, J., 2001. Coupling an advanced land surface hydrology model with the Penn State/NCAR MM5 modeling system. Part II. Preliminary model evaluation. Mon. Weather Rev. 129, 587–604.

Clapp, R.B., Hornberger, G.M., 1978. Empirical equations for some soil hydraulic properties. Water Resour. Res. 14, 601–604.

Coen, J., Mahalingam, S., Daily, J., 2004. Infrared imagery of crown-fire dynamics during FROSTFIRE. J. Appl. Meteorol. 43, 1241–1259.

Colle, B.A., Westrick, K.J., Mass, C.F., 1999. Evaluation of MM5 and Eta-10 precipitation forecasts over the Pacific Northwest during the cool season. Weather Forecast. 14, 137–154.

Copeland, J.H., Pielke, R.A., Kittel, T.G.F., 1996. Potential climatic impacts of vegetation change: a regional modeling study. J. Geophys. Res. 101D, 7409–7418.

Cosby, B.J., Hornberger, G.M., Clapp, R.B., Ginn, T.R., 1984. A statistical exploration of the relationships of soil moisture characteristics to the physical properties of soils. Water Resour. Res. 20, 682–690.

Crook, N.A., 1996. Sensitivity of moist convection forced by boundary layer processes to low-level thermodynamic fields. Mon. Weather Rev. 124, 1767–1785.

Deardorff, J.W., 1978. Efficient prediction of ground surface temperature and moisture, with inclusion of a layer of vegetation. J. Geophys. Res. 84, 1889–1903.

de Groot, S.R., 1951. Thermodynamics of irreversible processes. Interscience Publishers Inc., New York. 242 pp.

de Vries, D.A., 1958. Simultaneous transfer of heat and moisture in porous media. Trans. Am. Geophys. Union 39, 909–916.

Dingman, S.L., 1994. Physical Hydrology. Macmillan Publishing Company, New York. 575 pp.

DNR, Department of Natural Resources, Alaska Wildland fire coordination group, 2000. Fire and smoke in Alaska. U.S. Government printing office. 573-278/21012, region 8.

Doran, J.C., Zhong, S., 2000. A study of the effects of sub-grid-scale land use differences on atmospheric stability in prestorm environments. J. Geophys. Res. 105, 9381–9392.

Dudhia, J., 1989. Numerical study of convection observed during the winter monsoon experiment using a mesoscale two-dimensional model. J. Atmos. Sci. 46, 3077–3107.

Dudhia, J., 1993. A non-hydrostatic version of the Penn State-NCAR mesoscale model: validation tests and simulation of an Atlantic cyclone and cold front. Mon. Weather Rev. 121, 1493–1513.

Fan, X., Tilley, J.S., 2005. Dynamic assimilation of MODIS-retrieved humidity profiles within a regional model for high latitude forecast applications. Mon. Weather Rev. 133, 3450–3480.

Fehr, T., Dotzek, N., Hoeller, H., 2003. Comparison of lightning activity and radar-retrieved microphysical properties in EULINOX storms. Atmos. Res. 70, doi:10.1016/j.atmosres2004.11.027.

Flerchinger, G.N., Saxton, K.E., 1989. Simultaneous heat and water model of a freezing snow-residue-soil system. I. Theory and development. Trans. ASAE 32, 565–571.

Friedrich, K., Mölders, N., 2000. On the influence of surface heterogeneity on latent heat-fluxes and stratus properties. Atmos. Res. 54, 59–85.

Gabriel, H.W., Tande, G.F., 1983. A regional approach to fire history in Alaska, U.S. Department of the Interior, Bureau of Land Management-Alaska, Washington, DC: USDI Bureau of Land Management, Tech. Report 9, 33 pp.

Grell, G., Kuo, Y.-H., Pasch, R.J., 1991. Semi-prognostic tests of cumulus parameterization schemes in the middle latitudes. Mon. Weather Rev. 119, 5–31.

Grell, G., Dudhia, J., Stauffer, D., 1994. A description of the fifth-generation Penn State/NCAR Mesoscale Model (MM5), Technical Note, NCAR/TN-398+STR, 122 pp.

Gutman, G., Ignatov, A., 1998. The derivation of green vegetation from NOAA/AVHHRR data for use in numerical weather prediction models. Int. J. Remote Sens. 19, 1533.

Haltiner, G.J., Martin, F.L., 1957. Dynamical and Physical Meteorology. McGraw-Hill, New York/Toronto/London. 470 pp.

Hanna, S.R., 1994. Mesoscale meteorological model evaluation techniques with emphasis on needs of air quality models. In: Pielke, R.A., Pearce, R.P. (Eds.), Mesoscale Modeling of the Atmosphere, Meteorological Monographs, vol. 25, pp. 47–58.

Hess, J.C., Scott, C.A., Hufford, G.L., Fleming, M.D., 2001. El Nino and its impact on fire weather conditions in Alaska. J. Wildl. Fire 10, 1–13.

Hinzman, L.D., Fukuda, M., Sandberg, D.V., Chapin III, F.S., Dash, D., 2003. FROSTFIRE: an experimental approach to predicting the climate feedbacks from changing boreal fire regime. J. Geophys. Res. 108D, 8153, doi:10.1029/2001JD000415.

Hoadley, J.L., Westrick, K., Ferguson, S.A., Goodrick, S.L., Bradshaw, L., Werth, P., 2004. The effect of model resolution in predicting meteorological parameters used in fire danger rating. J. Appl. Meteorol. 43, 1333–1347.

Hong, S.-Y., Pan, H.-L., 1996. Nonlocal boundary layer vertical diffusion in a medium-range forecast model. Mon. Weather Rev. 124, 2322–2339.

Houze, R.A., 1993. Cloud dynamics. Academic Press, San Diego, p. 573.

Jackson, R.B., Canadell, J., Ehleringer, J.R., Mooney, H.A., Sala, O.E., Schulze, E.D., 1996. A global analysis of root distributions for terrestrial biomes. Oecologia 108, 389–411.

Kramm, G., 1995. Zum Austausch von Ozon und reaktiven Stickstoffverbindungen zwischen Atmosphäre und Biosphäre. Maraun-Verlag, Frankfurt, p. 268.

Kramm, G., Dlugi, R., Mölders, N., Müller, H., 1994. Numerical investigations of the dry deposition of reactive trace gases. In: Baldasano, J.M., Brebbia, C.A., Power, H., Zannetti, P. (Eds.), Air Pollution II, vol. 1. Computer Simulation, Computational Mechanics Publications, Southampton, Boston, pp. 285–307.

Kramm, G., Beier, N., Foken, T., Müller, H., Schröder, P., Seiler, W., 1996. A SVAT scheme for NO, NO_2, and O_3 — model description. Meteorol. Atmos. Phys. 61, 89–106.

Liu, H., Randerson, J.T., Lindfors, J., Chapin III, F.S., 2005. Changes in the surface energy budget after fire in boreal ecosystems of Interior Alaska: an annual perspective. J. Geophys. Res. 110, D13101, doi:10.1029/2004JD005158.

Lorenc, A.C., Barker, D., Bell, R.S., Macpherson, B., Maycock, A.J., 1996. On the use of radiosonde humidity observations in mid-latitude NWP. Meteorol. Atmos. Phys. 60, 3–17.

Lynn, B.H., Khain, A.P., Dudhia, J., Rosenfeld, D., Pokrovsky, A., Seifert, A., 2005a. Spectral (bin) microphysics coupled with a mesoscale model (MM5). Part I. Model description and first results. Mon. Weather Rev. 133, 44–58.

Lynn, B.H., Khain, A.P., Dudhia, J., Rosenfeld, D., Pokrovsky, A., Seifert, A., 2005b. Spectral (bin) microphysics coupled with a mesoscale model (MM5). Part II. Simulation of a CaPE rain event with a squall line. Mon. Weather Rev. 133, 59–71.

Mahrt, L., Sun, J., Vickers, D., MacPherson, J.I., Pederson, J.R., Desjardins, R., 1994. Observations of fluxes and inland breezes over a heterogeneous surface. J. Atmos. Sci. 51, 2165–2178.

Manning, W.K., Davis, C.A., 1997. Verification and sensitivity experiments for the WISP94 MM5 forecasts. Weather Forecast. 12, 719–735.

Miller, D.A., White, R.A., 1998. A conterminous United States Multilayer soil characteristics data set for regional climate and hydrological modeling. Earth Interactions 2. [Available on-line at http://EarthInteractions.org].

Mölders, N., 1999a. On the effects of different flooding stages of the Odra and different landuse types on the local distributions of evapotranspiration, cloudiness and rainfall in the Brandenburg–Polish border area. Contrib. Atmos. Phys. 72, 1–24.

Mölders, N., 1999b. On the atmospheric response to urbanization and open-pit mining under various geostrophic wind conditions. Meteorol. Atmos. Phys. 71, 205–228.

Mölders, N., 2000a. Application of the principle of superposition to detect nonlinearity in the short-term atmospheric response to concurrent land-use changes associated with future landscapes. Meteorol. Atmos. Phys. 72, 47–68.

Mölders, N., 2000b. HTSVS — a new land-surface scheme for MM5. The Tenth PSU/NCAR Mesoscale Model Users' Workshop, pp. 33–35.

Mölders, N., Olson, M.A., 2004. Impact of urban effects on precipitation in high-latitudes. J. Hydrometeorol. 5, 409–429.

Mölders, N., Walsh, J.E., 2004. Atmospheric response to soil–frost and snow in Alaska in March. Theor. Appl. Climatol. 77, 77–105.

Mölders, N., Haferkorn, U., Döring, J., Kramm, G., 2003a. Long-term numerical investigations on the water budget quantities predicted by the hydro-thermodynamic soil vegetation scheme (HTSVS). Part I. Description of the model and impact of long-wave radiation, roots, snow, and soil frost. Meteorol. Atmos. Phys. 84, 115–135.

Mölders, N., Haferkorn, U., Döring, J., Kramm, G., 2003b. Long-term numerical investigations on the water budget quantities predicted by the hydro-thermodynamic soil vegetation scheme (HTSVS). Part II. Evaluation, sensitivity, and uncertainty. Meteorol. Atmos. Phys. 84, 137–156.

Narapusetty, B., Mölders, N., 2005. Evaluation of snow depth and soil temperature predicted by the Hydro-Thermodynamic Soil Vegetation Scheme (HTSVS) coupled with the PennState/NCAR Mesoscale Meteorological Model (MM5). J. Appl. Meteorol. 44, 1827–1843.

Noppel, H., Fiedler, F., 2002. Mesoscale transport over complex terrain by slope winds — a conceptual model and numerical simulations. Boundary - Layer Meteorol. 104, 73–97.

Oke, T.R., 1978. Boundary Layer Climates. Routledge, London/ New York, p. 435.

Oncley, S.P., Dudhia, J., 1995. Evaluation of surface fluxes from MM5 using observations. Mon. Weather Rev. 123, 3344–3357.

O'Neal, M., 1996. Interactions between land cover and convective cloud cover over midwestern North America detected from GOES satellite data. Int. J. Remote Sens. 17, 1149–1181.

Pan, Z., Takle, E., Segal, M., Arritt, R., 1999. Simulation of potential impacts of man-made land use changes on U.S. summer climate under various synoptic regimes. J. Geophys. Res. 104D, 6515–6528.

Peckham, S.E., Wicker, L.J., 2000. The influence of topography and lower-troposphere winds on dryline morphology. Mon. Weather Rev. 128, 2165–2189.

Peckham, S.E., Wilhelmson, R.B., Wicker, L.J., Ziegler, C.L., 2004. Numerical simulation of the interaction between the dryline and horizontal convective roll. Mon. Weather Rev. 132, 1792–1812.

Philip, J.R., de Vries, D.A., 1957. Moisture in porous materials under temperature gradients. Trans. Am. Geophys. Soc. 18, 222–232.

Pielke Sr., R.A., 2001. Mesoscale Meteorological Modeling. Academic Press, London, p. 676.

Pielke, R.A., Walko, R.L., Steyaert, L.T., Vidale, P.L., Liston, G.E., Lyons, W.A., Chase, T.N., 1999. The influence of anthropogenic landscape changes on weather in South Florida. Mon. Weather Rev. 127, 1663–1673.

Pinty, J.P., Mascart, P., Richard, E., Rosset, R., 1989. An investigation of mesoscale flows induced by vegetation inhomogeneities using an evapotranspiration model calibrated against HAPEX-MOBILHY data. J. Appl. Meteorol. 28, 976–992.

Podur, J., Martell, D.L., Knight, K., 2002. Statistical quality control analysis of forest fire activity in Canada. Can. J. For. Res. 32, 195–205.

Prigogine, I., 1961. Introduction to Thermodynamics of Irreversible Processes. Interscience Publ. Inc., New York, London. 119 pp.

Rabin, R.M., Stadler, S., Wetzel, P.J., Stensrud, D.J., Gregory, M., 1990. Observed effects of landscape variability on convective clouds. Bull. Am. Meteorol. Soc. 71, 272–280.

Reisner, J., Rasmussen, R.M., Bruintjes, R.T., 1998. Explicit forecasting of supercooled liquid water in winter storms using the MM5 mesoscale model. Quart. J. R. Meteorol. Soc. 124B, 1071–1107.

Sasamori, T., 1970. A numerical study of atmospheric and soil boundary layers. J. Atmos. Sci. 27, 1122–1137.

Schmidt, B., 1990. Derivation of an explicit equation for infiltration on the basis of the Mein–Larson model. Hydrol. Sci. J. 35, 197–208.

Segal, M., Arritt, R.W., 1992. Nonclassical mesoscale circulations caused by surface sensible heat-flux gradients. Bull. Am. Meteorol. Soc. 73, 1593–1604.

Shuttleworth, W.J., 1988. Macrohydrology — the new challenge for process hydrology. J. Hydrol. 10, 31–56.

Sievers, U., Forkel, R., Zdunkowski, W., 1983. Transport equations for heat and moisture in the soil and their application to boundary layer problems. Contrib. Atmos. Phys. 56, 58–83.

Stocks, B.J., Fosberg, M.A., Lynham, T.J., Means, L., Wotton, B.M., Yang, Q., 1998. Climate change and forest fire potential in Russian and Canadian boreal forests. Clim. Change 38, 1–13.

Stocks, B.J., Fosberg, M.A., Wotten, M.B., Lynham, T.J., Ryan, K.C., 2000. Climate change and forest fire activity in North American boreal forests. In: Kasischke, E.S., Stocks, B.J. (Eds.), Fire, Climate Change, and Carbon Cycling in North American Boreal Forest. Springer, New York, pp. 368–376.

Taha, H., 1999. Modifying a mesoscale meteorological model to better incorporate urban heat storage: a bulk-parameterization approach. J. Appl. Meteorol. 38, 466–473.

Thompson, G., Rasmussen, R.M., Manning, K., 2004. Explicit forecasts of winter precipitation using an improved bulk microphysics scheme. Part I. Description and sensitivity analysis. Mon. Weather Rev. 132, 519–542.

Trier, S.B., Chen, F., Manning, K., 2004. A study of convection initiation in a mesoscale model using high-resolution land surface initial conditions. Mon. Weather Rev. 132, 2954–2976.

US Census Bureau, 2000. http://www.pbs.org/newshour/extra/features/jan-june01/census_newdata.html.

Weaver, C.P., Avissar, R., 2001. Atmospheric disturbances caused by human modification of the landscape. Bull. Am. Meteorol. Soc. 82, 269–281.

Westerling, A.L., Gershunov, A., Brown, T.J., Cayan, D.R., Dettinger, M.D., 2003. Climate and wildfire in the western United States. Bull. Am. Meteorol. Soc. 84, 595–604.

Wilson, M.F., Henderson-Sellers, A., Dickinson, R.E., Kennedy, P.J., 1987. Sensitivity of the biosphere–atmosphere transfer scheme (BATS) to the inclusion of variable soil characteristics. J. Clim. Appl. Meteorol. 26, 341–362.

Xue, Y., 1996. The impact of desertification in the Mongolian and the inner Mongolian grassland on the regional climate. J. Climate 9, 2173–2189.

Zhuang, Q., McGuire, A.D., Harden, J., O'Neill, K.P., Romanovsky, V.E., Yarie, J., 2003. Modeling soil thermal and carbon dynamics of a fire chronosequence in Interior Alaska. J. Geophys. Res. 108D, 8147, doi:10.1029/2001JD001244.

Ziegler, C.L., Martin, W.J., Pielke, R.A., Walko, R.L., 1995. A modeling study of the dryline. J. Atmos. Sci. 52, 263–285.

Ziegler, C.L., Lee, T.J., Pielke, R.A., 1997. Convective initiation at the dryline: a modeling study. Mon. Weather Rev. 125, 1001–1026.